Journal of Computational Physics 229 (2010) 4884–4906

Contents lists available at ScienceDirect

Journal of Computational Physics

journal homepage: www.elsevier.com/locate/jcp

A multislope MUSCL method on unstructured meshes applied to compressible Euler equations for axisymmetric swirling flows

S. Clain [a], D. Rochette [b], R. Touzani [c,d,*]

[a] Institut de Mathématiques, CNRS UMR 5219, Université Paul Sabatier Toulouse 3, 118 route de Narbonne, 31062 Toulouse Cedex 4, France
[b] Clermont Université, Université Blaise Pascal, Laboratoire Arc Électrique et Plasmas Thermiques, BP 10448, F-63000 Clermont-Ferrand, France
[c] Clermont Université, Université Blaise Pascal, Laboratoire de Mathématiques, BP 10448, F-63000 Clermont-Ferrand, France
[d] CNRS, UMR 6620, Laboratoire de Mathématiques, F-63177 Aubière, France

ARTICLE INFO

Article history:
Received 20 November 2008
Received in revised form 22 February 2010
Accepted 3 March 2010
Available online 23 March 2010

Keywords:
Axisymmetric compressible Euler equations
Swirling flow
Finite volumes
MUSCL method
Unstructured mesh

ABSTRACT

A finite volume method for the numerical solution of axisymmetric inviscid swirling flows is presented. The governing equations of the flow are the axisymmetric compressible Euler equations including swirl (or tangential) velocity. A first-order scheme is introduced where the convective fluxes at cell interfaces are evaluated by the Rusanov or the HLLC numerical flux while the geometric source terms are discretizated to provide a well-balanced scheme i.e. the steady-state solutions with null velocity are preserved. Extension to the second-order space approximation using a multislope MUSCL method is then derived. To test the numerical scheme, a stationary solution of the fluid flow following the radial direction has been established with a zero and nonzero tangential velocity. Numerical and exact solutions are compared for classical Riemann problems where we employ different limiters and effectiveness of the multislope MUSCL scheme is demonstrated for strongly shocked axially symmetric flows like in spherical bubble compression problem. Two other tests with axisymmetric geometries are performed: the supersonic flow in a tube with a cone and the axisymmetric blunt body with a free stream.

1. Introduction

Axisymmetric Euler system using cylindrical coordinates is used in numerous applications such as axisymmetric flows in a nozzle [14], supersonic jets [15], turbo machine modeling [11,23]. More recently, inductive plasma flows are modeled with the axisymmetric Euler formulation taking into account the tangential velocity, the so-called swirling flow [20,24]. An axisymmetric formulation avoids considering a full three-dimensional problem leading to a strong computational cost reduction and meshes are easier to generate.

From a numerical point of view, the finite volume method [6,8,10] is a popular technique to compute numerical approximations of the Euler system solution for axisymmetric geometries but most of the authors have neglected the swirl velocity which is of crucial importance in some applications such as the inductive plasma problem. A particular issue concerns the choice of the variables to conserve. In a first approach, the mean value approximation of any generic function v on cell C_i is performed by using the classical average

$$v_i \approx \frac{\int_{C_i} v\,drdz}{\int_{C_i} drdz}$$

* Corresponding author at: Clermont Université, Université Blaise Pascal, Laboratoire de Mathématiques, BP 10448, F-63000 Clermont-ferrand, France.
E-mail address: Rachid.Touzani@univ-bpclermont.fr (R. Touzani).

0021-9991/$ - see front matter © 2010 Elsevier Inc. All rights reserved.
doi:10.1016/j.jcp.2010.03.004

where we employ the measure (metric) $dr\,dz$ [5]. A second approach consists in computing the mean value using the measure $r\,dr\,dz$ [10]:

$$v_i \approx \frac{\int_{C_i} vr\,dr\,dz}{\int_{C_i} r\,dr\,dz}$$

which leads to a better formulation. Indeed, v_i corresponds to the mean value of v in the three-dimensional context, i.e., the mean value on the axisymmetric torus with section C_i. On the other hand, the formulation simplifies the boundary condition at $r = 0$ since a null flux value naturally derives from the flux integration and no additional constraint is required on the symmetry axis [10].

To provide an approximation of the solution of the axisymmetric Euler system, we use a fractional step technique where we split the formulation into a conservative homogeneous equation and the source term. To solve the conservative part, a standard technique consists in using a first-order solver (Rusanov, HLLC, Roe or Riemann solver) combined with a second-order reconstruction such as the MUSCL method [13,21] to improve accuracy. The classical MUSCL technique uses a piecewise linear reconstruction with a slope limiting procedure to ensure L^∞-stability. Then two new approximations are computed on both sides of each edge and are employed in the numerical flux evaluation. We propose here to use a new reconstruction technique: the multislope MUSCL method [2–4] where the reconstructed values are obtained using an approximation of specific directional derivatives instead of the full gradient. The main advantage is that the reconstruction can be rewritten as a one-dimensional MUSCL method at each interface leading to a simple and efficient scheme.

In the axisymmetric context, there are few numerical tests to validate the scheme for compressible Euler equations. For example, we are not able to compute the exact solution of the Riemann problem excepting in very particular situations. We propose a new numerical test for the swirling flow based on the steady-state situation. We manage to reduce the Euler system to an ordinary differential equation and a simple approximation based on the forward Euler scheme is proposed to provide an accurate numerical solution.

The organization of the paper is as follows. In Section 2, we present the governing Euler equations in cylindrical coordinates assuming rotational symmetry. In Section 3, we present the numerical scheme and its second-order extension using a multislope MUSCL method. In Section 4, we establish a stationary solution assuming that the flow depends only on the radial direction and that the axial velocity is null. Finally, we present numerical experiments to test the obtained scheme.

2. Axisymmetric Euler equations for swirling flows

We first present the compressible Euler equations using the cylindrical coordinates and simplify them under the axisymmetric invariance assumption. For any point $X = (x, y, z) \in \mathbb{R}^3$ we denote by (r, θ, z) the associated cylindrical coordinates. Let

$$\mathcal{P} = \mathbb{R}^+ \times \mathbb{R} = \{(r, z) \in \mathbb{R}^2;\ r \geqslant 0\}$$

denote an axial cut of the three-dimensional space (the set of parameters) and let Ω be an open set of $\mathcal{P}$. The open set $\widetilde{\Omega} \subset \mathbb{R}^3$ will denote the three-dimensional volume obtained by rotation around the axial direction 0z, i.e.

$$\widetilde{\Omega} := \{(r\cos\theta, r\sin\theta, z);\ (r, z) \in \Omega,\ 0 \leqslant \theta < 2\pi\}.$$

We start by giving the compressible Euler equations in the domain $\widetilde{\Omega}$:

$$\frac{\partial \rho}{\partial t} + \nabla \cdot (\rho \mathbf{u}) = 0, \tag{1}$$

$$\frac{\partial (\rho \mathbf{u})}{\partial t} + \nabla \cdot (\rho \mathbf{u} \otimes \mathbf{u} + P\mathbf{I}) = 0, \tag{2}$$

$$\frac{\partial E}{\partial t} + \nabla \cdot ((E + P)\mathbf{u}) = 0, \tag{3}$$

where ρ is the fluid mass density, P is the pressure, $\mathbf{u}$ is the velocity vector and E is the total energy per unit volume. The tensors $\mathbf{u} \otimes \mathbf{u}$ and $\mathbf{I}$ stand for the tensor product of $\mathbf{u}$ by $\mathbf{u}$ and the unit tensor respectively.

To close the system, we add a state equation which in general form reads

$$P = \hat{P}(\rho, e),$$

where e stands for the specific internal energy related to the total energy by

$$E = \rho e + \frac{1}{2}\rho |\mathbf{u}|^2.$$

In the following, we restrict ourselves to an ideal gas, that is,

$$P = (\gamma - 1)\rho e, \tag{4}$$

where γ is the ratio of specific heats at constant pressure and volume.

We introduce the mapping defining cylindrical coordinates:

$$(r,\theta,z)\mapsto(r\cos\theta, r\sin\theta, z).$$

To any scalar function $f:\widetilde{\Omega}\to\mathbb{R}$, we associate the function $\widetilde{f}(r,\theta,z)=f(r\cos\theta,r\sin\theta,z)$ for $(r,z)\in\Omega$ and $\theta\in[0,2\pi)$. Due to the axial symmetry we look for solutions (density, velocity, pressure, etc.) that are independent of θ, i.e. all the involved functions will depend on space variables r and z and on the time variable t.

For the sake of simplicity, we shall omit the tilde symbol on the functions $f=f(r,z)$. Applying the divergence operator in cylindrical coordinates and eliminating the θ-derivatives, we deduce from (1)–(3) the following system (see Appendix B in [10] for the derivation details):

$$\frac{\partial\rho}{\partial t}+\frac{1}{r}\frac{\partial}{\partial r}(r\rho u_r)+\frac{\partial}{\partial z}(\rho u_z)=0, \tag{5}$$

$$\frac{\partial}{\partial t}(\rho u_r)+\frac{\partial}{\partial r}(\rho u_r^2+P)+\frac{\partial}{\partial z}(\rho u_r u_z)+\frac{1}{r}\rho(u_r^2-u_\theta^2)=0, \tag{6}$$

$$\frac{\partial}{\partial t}(\rho u_z)+\frac{\partial}{\partial r}(\rho u_z u_r)+\frac{\partial}{\partial z}(\rho u_z^2+P)+\frac{1}{r}\rho u_z u_r=0, \tag{7}$$

$$\frac{\partial}{\partial t}(\rho u_\theta)+\frac{\partial}{\partial r}(\rho u_\theta u_r)+\frac{\partial}{\partial z}(\rho u_\theta u_z)+\frac{2}{r}\rho u_\theta u_r=0, \tag{8}$$

$$\frac{\partial E}{\partial t}+\frac{1}{r}\frac{\partial}{\partial r}(ru_r(E+P))+\frac{\partial}{\partial z}(u_z(E+P))=0. \tag{9}$$

Note that assuming rotational symmetry naturally reduce the space dimension but does not reduce the number of unknowns since the velocity field has three nonzero components that are respectively the radial $u_r(r,z)$, the tangential $u_\theta(r,z)$ and the axial component $u_z(r,z)$.

To derive a conservative form of the system, we multiply Eqs. (5)–(9) by the radial coordinate r like in [8,18] and obtain then the final form of the Euler equations:

$$\frac{\partial}{\partial t}(r\rho)+\frac{\partial}{\partial r}(r\rho u_r)+\frac{\partial}{\partial z}(r\rho u_z)=0, \tag{10}$$

$$\frac{\partial}{\partial t}(r\rho u_r)+\frac{\partial}{\partial r}(r\rho u_r^2+rP)+\frac{\partial}{\partial z}(r\rho u_r u_z)=\rho u_\theta^2+P, \tag{11}$$

$$\frac{\partial}{\partial t}(r\rho u_z)+\frac{\partial}{\partial r}(r\rho u_z u_r)+\frac{\partial}{\partial z}(r\rho u_z^2+rP)=0, \tag{12}$$

$$\frac{\partial}{\partial t}(r\rho u_\theta)+\frac{\partial}{\partial r}(r\rho u_\theta u_r)+\frac{\partial}{\partial z}(r\rho u_\theta u_z)=-\rho u_\theta u_r, \tag{13}$$

$$\frac{\partial}{\partial t}(rE)+\frac{\partial}{\partial r}(ru_r(E+P))+\frac{\partial}{\partial z}(ru_z(E+P))=0. \tag{14}$$

Equivalently, we can write this system under the conservative form:

$$\frac{\partial(rU)}{\partial t}+\frac{\partial(rF_r(U))}{\partial r}+\frac{\partial(rF_z(U))}{\partial z}=G(U), \tag{15}$$

where U is the conservative variable vector defined by

$$U=\begin{pmatrix}\rho\\ \rho u_r\\ \rho u_z\\ \rho u_\theta\\ E\end{pmatrix},$$

and the fluxes $F_r(U)$ and $F_z(U)$ and the geometric source term $G(U)$ are given by:

$$F_r(U)=\begin{pmatrix}\rho u_r\\ \rho u_r^2+P\\ \rho u_z u_r\\ \rho u_\theta u_r\\ u_r(E+P)\end{pmatrix},\quad F_z(U)=\begin{pmatrix}\rho u_z\\ \rho u_r u_z\\ \rho u_z^2+P\\ \rho u_\theta u_z\\ u_z(E+P)\end{pmatrix},\quad G(U)=\begin{pmatrix}0\\ \rho u_\theta^2+P\\ 0\\ -\rho u_\theta u_r\\ 0\end{pmatrix}.$$

Clearly, the formulation (15) involves a divergence form in the left-hand side and the remaining terms are considered as source terms on the right-hand side.

3. A finite volume scheme with multislope MUSCL reconstruction

3.1. A first-order finite volume scheme

To address numerical approximation, we describe the finite volume method we use for the conservative part of the Euler system. We consider a conforming unstructured mesh of the two-dimensional domain Ω, made of triangles (or cells) $C_i\subset\Omega$,

$i = 1, \dots, n_c$. We denote by $v(i)$ the set of labels of the neighboring triangles C_j which share a common edge S_{ij} with the cell C_i and by $\mathbf{n}_{ij} = (n_{ij,r}, n_{ij,z})$ the outward unit normal vector to C_i.

We first integrate the system (15) over the cell C_i and use the Green formula to get

$$\frac{d}{dt}\int_{C_i} U(r,z,t)\, r\, dr\, dz + \int_{\partial C_i} \big(F_r(U) n_{ij,r} + F_z(U) n_{ij,z}\big) r\, d\sigma = \int_{C_i} G(U)\, dr\, dz,$$

where ∂C_i denotes the boundary of the cell C_i. Let $(t^n = n\,\Delta t)_{n\in\mathbb{N}}$ be a uniform subdivision of the time interval $[0, +\infty)$. Integrating on the interval $[t^n, t^{n+1}]$ we obtain the equation:

$$\int_{C_i} U(r,z,t^{n+1})\, r\, dr\, dz = \int_{C_i} U(r,z,t^n)\, r\, dr\, dz - \int_{t^n}^{t^{n+1}} \int_{\partial C_i} \big(F_r(U)\, n_{ij,r} + F_z(U)\, n_{ij,z}\big) r\, d\sigma\, dt + \int_{t^n}^{t^{n+1}} \int_{C_i} G(U)\, dr\, dz\, dt.$$

We aim at computing a constant piecewise approximation of the solution U on each cell C_i. To this end, U_i^n represents an approximation of the average of U on C_i at time t^n. More precisely, for a given cell C_i, we introduce the following measures

$$|C_i| = \int_{C_i} dr\, dz, \quad |C_i|_r = \int_{C_i} r\, dr\, dz,$$

and we define the approximation

$$U_i^n \approx \frac{1}{|C_i|_r} \int_{C_i} U(r,z,t^n)\, r\, dr\, dz. \tag{16}$$

In the same way, we define the measures of an edge

$$|S_{ij}| = \int_{S_{ij}} d\sigma, \quad |S_{ij}|_r = \int_{S_{ij}} r\, d\sigma,$$

and we define the approximation of the flux across the interface S_{ij} during the interval $[t^n, t^{n+1}]$ by

$$F_{ij}^n \approx \frac{1}{\Delta t\, |S_{ij}|_r} \int_{t^n}^{t^{n+1}} \int_{S_{ij}} (F_r(U)\, n_{ij,r} + F_z(U)\, n_{ij,z})\, r\, d\sigma\, dt.$$

We eventually build an approximation of the right-hand side contribution by

$$G_i^n \approx \frac{1}{\Delta t\, |C_i|} \int_{t^n}^{t^{n+1}} \int_{C_i} G(U)\, dr\, dz\, dt.$$

It results from (15) that the integrals involve two kinds of measures: $r\,dr\,dz$ and $dr\,dz$. To compute the mean value on the cell C_i employing the $r\,dr\,dz$ measure, we have to divide by $|C_i|_r$ since the approximation (16) becomes an equality for constant functions. On the other hand, we divide by $|C_i|$ to provide a mean value of G_i^n since we use the $dr\,dz$ measure in the integral (see [10, p. 495]).

To define an explicit scheme, we use a numerical flux such that

$$F_{ij}^n = \mathcal{F}(U_i^n, U_j^n, \mathbf{n}_{ij}), \quad G_i^n = G(U_i^n).$$

The scheme reads then

$$|C_i|_r U_i^{n+1} = |C_i|_r U_i^n - \Delta t \sum_{j\in v(i)} |S_{ij}|_r\, \mathcal{F}(U_i^n, U_j^n, \mathbf{n}_{ij}) + \Delta t\, |C_i|\, G(U_i^n). \tag{17}$$

In the present study, we present two numerical fluxes. We first use the Rusanov flux

$$\mathcal{F}(U_i, U_j, \mathbf{n}_{ij}) = \frac{F_r(U_i) + F_r(U_j)}{2}\, n_{ij,r} + \frac{F_z(U_i) + F_z(U_j)}{2}\, n_{ij,z} - \lambda_{ij}(U_j - U_i)$$

with $\lambda_{ij} = \lambda(U_i, U_j)$ large enough to ensure stability (see [18]). The main advantage of such a flux is its ability to handle real gases. The drawbacks are on one hand a significant diffusion amount and, on the other hand, contact discontinuities are not well approximated when steady-state problems are considered (see [18, p. 293,1,9, p. 204]). We then resort to two less diffusive numerical flux: the HLL and HLLC fluxes (see [18] for a technical description). Better resolution of the contact discontinuity for stationary solutions are obtained with the HLLC version while flux computations remain reasonable for complex applications (real gas, multispecies and multiphase problems for instance).

A first issue for the design of a numerical scheme is the preservation of steady-states. We only focus on the situation where the gas is at rest and prove that the scheme (17) preserves null velocity.

Let us give a new expression of (17) that uses the $|C_i|$ and $|S_{ij}|$ measures only. For a given triangle C_i, let $(r_{i,1}, z_{i,1}), (r_{i,2}, z_{i,2}), (r_{i,3}, z_{i,3})$ stand for the coordinates of its three vertexes. A similar notation is used for a given edge S_{ij}. Using the identities

$$|C_i|_r = |C_i|\,\frac{(r_{i,1}+r_{i,2}+r_{i,3})}{3}, \quad |S_{ij}|_r = |S_{ij}|\,\frac{(r_{ij,1}+r_{ij,2})}{2},$$

we obtain from (17)

$$U_i^{n+1} = U_i^n - \Delta t \sum_{j\in v(i)} \frac{|S_{ij}|}{|C_i|}\,\frac{3(r_{ij,1}+r_{ij,2})}{2(r_{i,1}+r_{i,2}+r_{i,3})}\,\mathcal{F}(U_i^n, U_j^n, \mathbf{n}_{ij}) + \frac{3\Delta t}{r_{i,1}+r_{i,2}+r_{i,3}}\,G(U_i^n).$$

Let us consider the initial condition U^0 where the pressure P^0 and the density ρ^0 are constant and the velocity is null, the resulting numerical flux is given by

$$\mathcal{F}(U_i^0, U_j^0, \mathbf{n}_{ij}) = \begin{pmatrix} 0 \\ P^0 n_{ij,r} \\ P^0 n_{ij,z} \\ 0 \\ 0 \end{pmatrix}.$$

We easily deduce that we have after the first step $\rho_i^1 = \rho^0$, $u_{\theta,i}^0 = u_{\theta,i}^1 = 0$ and $E_i^1 = E^0$ since the first and the two last components of vector G are null.

It remains to study radial and axial components of the velocity $u_{r,i}^1$ and $u_{z,i}^1$. From the momentum equations, the flux contribution is

$$\mathbf{C}_{\text{flux}} = \sum_{j\in v(i)} \frac{|S_{ij}|}{|C_i|}\,\frac{3(r_{ij,1}+r_{ij,2})}{2(r_{i,1}+r_{i,2}+r_{i,3})}\,P^0\,\mathbf{n}_{ij} = \frac{P^0}{|C_i|_r}\sum_{j\in v(i)} |S_{ij}|_r\,\mathbf{n}_{ij} = \frac{P^0}{|C_i|_r}\sum_{j\in v(i)}\int_{S_{ij}} r\,\mathbf{n}_{ij}\,d\sigma.$$

Using the Green formula we obtain

$$\mathbf{C}_{\text{flux}} = \frac{P^0}{|C_i|_r}\int_{C_i} \nabla_{r,z}(r)\,dr\,dz = P^0\,\frac{|C_i|}{|C_i|_r}\begin{pmatrix}1\\0\end{pmatrix}.$$

The right-hand side term for the radial and axial equations reduces to

$$\mathbf{C}_{\text{rhs}} = \frac{3}{r_{i,1}+r_{i,2}+r_{i,3}}P^0\begin{pmatrix}1\\0\end{pmatrix} = \frac{|C_i|}{|C_i|_r}P^0\begin{pmatrix}1\\0\end{pmatrix}.$$

Since $\mathbf{C}_{\text{flux}} = \mathbf{C}_{\text{rhs}}$, then $u_{r,i}^n = u_{z,i}^n = 0$ and the gas is at rest.

3.2. A second-order scheme using the multislope MUSCL method

In the early 70's, Van Leer [21] introduced the MUSCL technique (Monotonic Upwind Schemes for Conservation Laws) to get a more accurate approximation with less diffusion effect while maintaining stability. Extensions to multidimensional situations for unstructured meshes have been proposed (see [13,9]). We present here a new extension of the MUSCL technique on triangles where we use approximations of the directional derivative of U as proposed instead of an approximation of ∇U. Unlike the classical MUSCL method, we do not intend to reconstruct an approximation (a linear reconstruction, say) on the whole cell since we only need the two values u_{ij} and u_{ji} on both sides of the interface S_{ij} to achieve the finite volume algorithm.

We briefly introduce the multislope MUSCL method for a comprehensive description of the technique and we refer to [2–4] for details. The goal is to compute a more accurate flux $\mathcal{F}(U_{ij}^n, U_{ji}^n, \mathbf{n}_{ij})$ where U_{ij}^n and U_{ji}^n are better approximations of U on both sides of the edge S_{ij}. In the following, we shall skip the time index n for the sake of simplicity.

3.2.1. The fundamental decomposition

For a given volume C_i, we denote by $\mathbf{B}_i$ the centroid and $\mathbf{Q}_{ij}$ the intersection of the segment $[\mathbf{B}_i, \mathbf{B}_j]$ with the common edge S_{ij} for all $j \in v(i)$ (see Fig. 1).

We introduce the barycentric coordinates $(\rho_{ij})_{j\in v(i)}$, defined by

$$\sum_{j\in v(i)} \rho_{ij}\mathbf{B}_j = \mathbf{B}_i, \quad \sum_{j\in v(i)} \rho_{ij} = 1. \tag{18}$$

We assume that the point $\mathbf{B}_i$ is strictly inside the triangle formed by the three other points. Therefore $\rho_{ij} > 0$. Note that such a property is usually satisfied for Delaunay meshes. Defining the normalized direction

$$\mathbf{t}_{ij} = \frac{\mathbf{B}_i\mathbf{B}_j}{|\mathbf{B}_i\mathbf{B}_j|}$$

and using (18), we obtain a decomposition (referred to as the fundamental decomposition) of $\mathbf{t}_{ij}$ as a function of the two other directions:

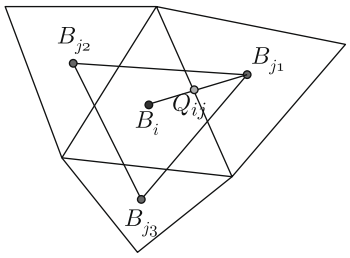

Fig. 1. Geometric ingredients and notations.

$$\mathbf{t}_{ij} = \sum_{\substack{k\in v(i)\\ k\neq j}} \beta_{ijk}\mathbf{t}_{ik}, \tag{19}$$

with the explicit expression of the β coefficients:

$$\beta_{ijk} = -\frac{\rho_{ik}}{\rho_{ij}}\frac{|\mathbf{B}_i\mathbf{B}_k|}{|\mathbf{B}_i\mathbf{B}_j|}.$$

3.2.2. The slope limiter

We now focus on the reconstruction of U_{ij}. To this end, we consider the physical variable vector

$$V = \begin{pmatrix} \rho \\ u_r \\ u_z \\ u_\theta \\ P \end{pmatrix},$$

and denote by v a generic component of the vector V, i.e. $v = \rho, u_r, u_z, u_\theta$ or P. We construct a first set of slopes, that will be referred to as *downstream slopes*

$$p_{ij}^{+} = \frac{v_j - v_i}{|\mathbf{B}_i\mathbf{B}_j|} \quad \text{for all } i, \quad 1 \leqslant i \leqslant n_c,\ j \in v(i).$$

The slopes represent an approximation of the directional derivative along $\mathbf{t}_{ij}$. We define the *upstream slopes* by

$$p_{ij}^{-} = \sum_{\substack{k\in v(i)\\ k\neq j}} \beta_{ijk}p_{ik}^{+} \quad \text{for all } i, \quad 1 \leqslant i \leqslant n_c,\ j \in v(i).$$

The vector $\mathbf{t}_{ij}$ gives an orientation and the upstream and downstream notions are defined with respect to the point $\mathbf{B}_i$ and the $\mathbf{t}_{ij}$ direction (like a virtual flow moving with the $\mathbf{t}_{ij}$ velocity). Indeed, assume that an observer located at point $\mathbf{B}_i$ looks in direction $\mathbf{t}_{ij}$, the slope p_{ij}^{+} is the downstream slope because it corresponds to informations coming in front of the observer whereas p_{ij}^{-} is the upstream slope because the information come behind the observer.

We finally compute the slopes p_{ij} using a limiting procedure, for example

$$p_{ij} = \text{minmod}\,(p_{ij}^{+}, p_{ij}^{-}).$$

Other limiters have been tested in the numerical section. Obviously, we have to construct five slopes p_{ij}, one for each variable. We eventually construct the new value v_{ij} by setting

$$v_{ij} = v_i + p_{ij}\,|\mathbf{B}_i\mathbf{Q}_{ij}|. \tag{20}$$

With V_{ij} and V_{ji} in hand, we compute the conservative variable vector U_{ij} and U_{ji} on both sides of the interface S_{ij} to provide the flux evaluation $\mathcal{F}(U_{ij}, U_{ji}, \mathbf{n}_{ij})$.

Remark 1. Thanks to the fundamental decomposition (19) we can prove that the reconstruction is exact for linear functions, i.e. $v(Q_{ij}) = v_{ij}$, if v is piecewise linear. Other choices for the collocation point $\mathbf{Q}_{ij}$ have been tested in Clauzon [4].

Remark 2. Computational cost and accuracy comparisons have been made between the multislope methods and classical MUSCL methods for two-dimensional geometries [2] and three-dimensional geometries [4]. In [4, pp. 109–111], a convergence rate of $\mathcal{O}(h^{1.2})$ is obtained with the multislope approach whereas the classical method gives a $\mathcal{O}(h^{0.8})$ using the Barth limiter. Furthermore, numerical experiments in the three dimensional context for the advection problem show, that to

obtain the same prescribed precision, the classical second-order scheme is 16 times faster than the first-order scheme while the ratio is 1130 when the multislope method is used see [4, p. 115].

Remark 3. The positivity of the barycentric coordinates implies that $\beta_{ijk} < 0$. An important consequence is that if v_i is a local extremum then $p_{ij}^+ p_{ij}^- \leqslant 0$. This implies $p_{ij} = 0$, which prevents the extrema from increasing (see [3]). We have observed that all Delaunay meshes we have employed provide positive barycentric coordinates for any elements.

Remark 4. The main issue is that we consider only one-dimensional reconstruction in each direction. This enables using any classical 1D limiter to compute the slope p_{ij} (see [4] for more details). In the case where C_i has a common edge with the boundary, we set $p_{ij} = 0$ which results in a first–order scheme.

Remark 5. It is important to perform the reconstruction with the physical variables instead of the conservative variables. Indeed, in some situations a reconstruction based on the conservative variables can yield a negative internal energy since it is obtained by subtracting the kinetic energy from the total energy.

4. Steady-state radial solutions

Let us investigate the particular case of steady-state radial solutions. This case is helpful in the sense that it provides a reference solution to test the chosen numerical scheme. In practice, a stationary solution is obtained by supplying adequate boundary conditions to the time dependent problem and letting the solution converge to a stationary state. In addition, as far as some compressible flows for industrial applications like in induction plasma problems (see [22] for instance) are concerned, stationary solutions are to be considered.

It turns out that it is rather difficult to compute an exact solution for stationary flows. To provide a simple case, we resort to restrict this section to radial solutions, i.e. that do not depend on z and such that $u_z = 0$. Under these assumptions, Eqs. (11)–(14) reduce to:

$$\frac{d}{dr}(r\rho u_r) = 0, \tag{21}$$

$$\frac{d}{dr}\left(r(\rho u_r^2 + P)\right) = \rho u_\theta^2 + P, \tag{22}$$

$$\frac{d}{dr}(r\rho u_\theta u_r) = -\rho u_\theta u_r, \tag{23}$$

$$\frac{d}{dr}(r u_r(E + P)) = 0. \tag{24}$$

Using the state equation of an ideal gas (4), the integration of Eqs. (21), (23) and (24) gives:

$$\rho u_r = \frac{\alpha_1}{r}, \tag{25}$$

$$\rho u_\theta u_r = \frac{\alpha_2}{r^2}, \tag{26}$$

$$u_r\left(\frac{\gamma}{\gamma - 1}P + \frac{1}{2}\rho(u_r^2 + u_\theta^2)\right) = \frac{\alpha_3}{r}, \tag{27}$$

where α_1, α_2 and α_3 are constants.

Thanks to relations (25) and (26), the expression of the tangential velocity u_θ becomes

$$u_\theta = \frac{\alpha_2}{\alpha_1 r}. \tag{28}$$

Let us introduce two new variables: $a = \rho u_r^2$ and $b = \rho u_\theta^2$. The system becomes then:

$$\begin{cases} ab = \frac{\alpha_2^2}{r^4}, \\ \frac{\gamma}{\gamma-1}P + \frac{1}{2}(a + b) = \frac{\alpha_1\alpha_3}{ar^2}, \\ \frac{d(a+P)}{dr} = \frac{b-a}{r}. \end{cases} \tag{29}$$

Let us show how to reduce the system (29) to an ordinary differential equation that we solve numerically. We first deal with the simple case where $u_\theta = 0$, i.e. $b = 0$. Then, we consider the more general case of a swirling flow.

4.1. First case: $u_\theta = 0$

Let us first consider the case where the fluid flow has the property $u_\theta = 0$. Then system (29) is reduced to:

$$\begin{cases} \frac{\gamma}{\gamma-1}P + \frac{1}{2}a = \frac{\alpha_1\alpha_3}{ar^2}, \\ \frac{d(a+P)}{dr} = -\frac{a}{r}. \end{cases} \tag{30}$$

From this we deduce

$$\frac{d}{dr}\left(\frac{\gamma-1}{\gamma}\frac{\alpha_1\alpha_3}{ar^2}+\frac{\gamma+1}{2\gamma}a\right)=-\frac{a}{r}.$$

Therefore

$$a'=-\frac{a}{r}\frac{2A-1}{A-\frac{\gamma+1}{2\gamma}}, \tag{31}$$

where

$$A=\frac{\gamma-1}{\gamma}\frac{\alpha_1\alpha_3}{a^2r^2}=\frac{\gamma-1}{\gamma}\frac{\alpha_3}{\alpha_1^3}r^2\rho^2.$$

By differentiating the identity $\alpha_1^2=r^2\rho a$, we deduce

$$\frac{d\rho}{dr}=-\alpha_1^2\left(\frac{2a+ra'}{r^3a^2}\right).$$

From (31), we get

$$\frac{d\rho}{dr}=\frac{\alpha_1^2}{\gamma ar^3}\left(\frac{1}{A-\frac{\gamma+1}{2\gamma}}\right).$$

This eventually gives the ordinary differential equation for the density:

$$\frac{d\rho}{dr}=\frac{\rho}{\left(\frac{\alpha_3}{\alpha_1^3}\rho^2r^2-\frac{\gamma+1}{2(\gamma-1)}\right)(\gamma-1)r}. \tag{32}$$

The numerical solution of Eq. (32) is described in Section 4.3.

Remark 6. An analytical solution of Eq. (32) can be obtained if we assume that

$$\frac{\alpha_3}{\alpha_1^3}\rho^2r^2\gg\frac{\gamma+1}{2(\gamma-1)}.$$

This assumption is valid in particular for subsonic flows at ambient temperature for instance. Neglecting the higher order term, the differential Eq. (32) reduces to

$$2\rho\frac{d\rho}{dr}=\frac{2\alpha_1^3}{(\gamma-1)\alpha_3r^3}.$$

Using the initial condition $\rho(r=R_0)=\rho_0$, we obtain the solution

$$\rho(r)=\sqrt{\rho_0^2+\frac{\alpha_1^3}{\alpha_3(\gamma-1)}\left(\frac{1}{R_0^2}-\frac{1}{r^2}\right)}. \tag{33}$$

4.2. The general case (swirling flow)

We now deal with the general case where $u_\theta\neq 0$. Differentiating the first equation of the system (29) yields

$$ba'+ab'=-\frac{4ab}{r}. \tag{34}$$

Thus

$$b'=-\frac{ba'}{a}-\frac{4b}{r}. \tag{35}$$

Let us substitute P in the system (29) and use (34) and (35). We get

$$\frac{d}{dr}\left(\frac{\gamma-1}{\gamma}\frac{\alpha_1\alpha_3}{ar^2}-\frac{\gamma-1}{2\gamma}b+\frac{\gamma+1}{2\gamma}a\right)=\frac{b-a}{r}.$$

Expressing the derivative of the previous expression and using (35), we get

$$\frac{\gamma-1}{\gamma a}\left(\frac{b}{2}-\frac{\alpha_1\alpha_3}{ar^2}+\frac{a(\gamma+1)}{2(\gamma-1)}\right)a'=\frac{a}{r}\left(\frac{b}{a}-\frac{\gamma-1}{\gamma a}\left(\frac{4b}{2}-\frac{2\alpha_1\alpha_3}{ar^2}\right)-1\right). \tag{36}$$

Since $\alpha_1^2 = r^2\rho a$, we obtain

$$\frac{d\rho}{dr} = -\alpha_1^2\left(\frac{2ra + r^2a'}{r^4a^2}\right). \tag{37}$$

After calculation, (36) and (37) give

$$\frac{d\rho}{dr} = -\frac{\alpha_1^2}{ar^3}\left(\frac{a+b}{(\gamma-1)\left(\frac{b}{2} - \frac{\alpha_1\alpha_3}{ar^2}\right) + \frac{(\gamma+1)}{2}a}\right).$$

Using the definitions of ρ and P, we finally obtain the ordinary differential equation for the fluid density:

$$\frac{d\rho}{dr} = \frac{\rho}{r}\left(\frac{a+b}{\gamma P - a}\right). \tag{38}$$

Remark 7. In Eq. (38), the functions a, b, P depend only on ρ, r and the constants. Indeed, for a given ρ, we can compute $b = \rho u_\theta^2$ using (28). We then deduce a with the first relation of system (29). We finally compute P with the help of the second relation of system (29).

4.3. A numerical method for stationary radial solutions

We consider a uniform subdivision of the domain $[R_0, R_1]$ with K elements where $r_k = R_0 + k\Delta r, k = 0, \ldots, K$ with $\Delta r = (R_1 - R_0)/K$. To avoid the singularity at $r = 0$, we have taken $R_0 > 0$. To obtain an approximation of the density ρ for Eqs. (32) and (38), we use the explicit Euler scheme:

$$\text{case } u_\theta = 0: \ \rho_{k+1} = \rho_k + \Delta r \frac{\rho_k}{\left(\frac{\alpha_3}{\alpha_1^2}\rho_k^2 r_k^2 - \frac{\gamma+1}{2(\gamma-1)}\right)(\gamma-1)r_k}, \tag{39}$$

$$\text{case } u_\theta \neq 0: \ \rho_{k+1} = \rho_k + \Delta r \frac{\rho_k}{r_k}\left(\frac{a_k + b_k}{\gamma P_k - a_k}\right). \tag{40}$$

The other parameters, namely the radial velocity u_r, the tangential velocity u_θ and the pressure P, are deduced using:

$$u_{r,k+1} = \frac{\alpha_1}{\rho_{k+1} r_{k+1}},$$
$$u_{\theta,k+1} = \frac{\alpha_2}{\alpha_1 r_{k+1}},$$
$$P_{k+1} = \frac{\gamma-1}{\gamma}\left(\frac{\alpha_1\alpha_3}{\rho_{k+1}u_{r,k+1}^2 r_{k+1}^2} - \frac{1}{2}\rho_{k+1}(u_{r,k+1}^2 + u_{\theta,k+1}^2)\right).$$

The values of a and b are then updated by:

$$a_{k+1} = \rho_{k+1}u_{r,k+1}^2,$$
$$b_{k+1} = \rho_{k+1}u_{\theta,k+1}^2.$$

5. Numerical tests

We have realized several series of numerical experiments to confirm the efficiency of the proposed numerical method. The first collection of tests concerns some standard academic problems to check convergence and accuracy properties of the schemes developed throughout this paper whereas the second collection presents more complex numerical simulations of practical interest. The first series of tests concerns the preservation property where we show that the algorithm preserves the situation when the gas is at rest which proves that the well-balancing property is satisfied. A second series of tests concerns radial steady-state solutions. We observe convergence for large time to the stationary solution computed with the numerical method proposed in Section 4.3. A third series of numerical experiments is devoted to the Riemann problem. We impose an initial condition made of two constant states for $z < 1/2$ and $z > 1/2$ such that we obtain a classical one-dimensional Sod tube problem in the Oz-direction. We then compare the numerical solutions to the analytical ones and several limiters are compared in the double rarefaction case.

A more complex test concerns the converging spherical shock [8] simulating compression of a gas bubble. This test problem allows checking the capacity of the numerical scheme to preserve spherical symmetry of the problem.

Finally, we describe two more significant test problems. The first one is the supersonic flow test in a tube with a cone with a swirl velocity. The second test is the axisymmetric blunt body [12,6]. Computations have been carried out using the finite element/finite volume library OFELI [19].

5.1. Conservation of the gas at rest

We consider the domain $\Omega = [0,1] \times [0,1]$ covered by a uniform mesh of 40 squares divided in four triangles (Scottish mesh) as displayed in Figs. 2 and 3.

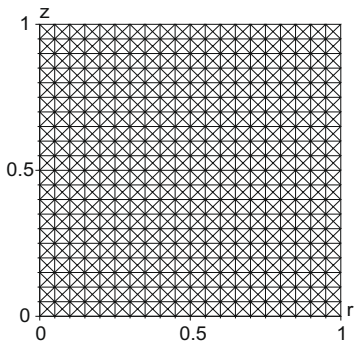

Fig. 2. The Scottish mesh.

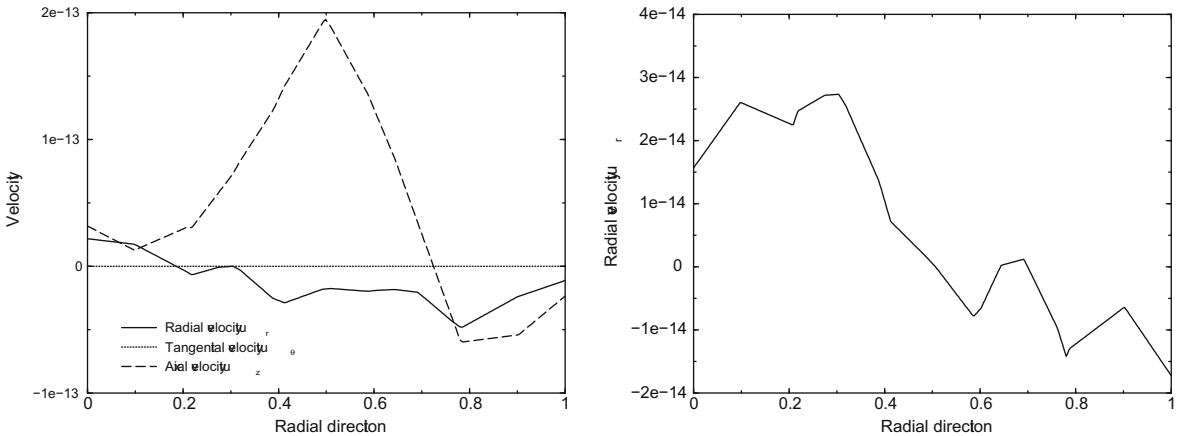

Fig. 3. Radial, axial and tangential velocity distribution at $z = 0.5$ for the first test (left) and radial velocity at $z = 0.5$ for the second test (right).

We solve the Euler system using the HLLC numerical flux where we prescribe $P = 10^5$ for the pressure and $\rho = 1.2$ for the density as initial conditions. In the first test, we assume that the gas is initially at rest ($u_r = u_\theta = u_z = 0$) while we consider a second test where the initial axial velocity is $u_z = 100$. On the boundaries $r = 0$ and $r = 1$ we impose a reflection condition using the ghost-cell technique [18] and a Dirichlet condition for the boundaries $z = 0$ and $z = 1$ equal to the initial condition. In both situations, we observe the preservation of the gas at rest. A few numerical artifacts of order 10^{-14} which correspond to the computer precision are present.

5.2. Stationary solution

The goal of this series of tests is to study steady-state radial solution approximations and show that any non-stationary solution of the system (15) using convenient boundary conditions U_{inlet} and U_{outlet} converges asymptotically to the stationary solution.

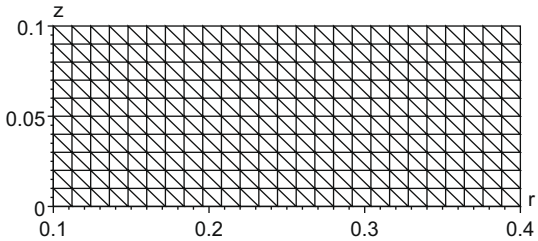

Fig. 4. Example of mesh used for the stationary solution.

To compute the stationary solution using the proposed technique in Section 4.3, we consider a subdivision following the one-dimensional radial direction ($R_0 = 0.1, R_1 = 0.4$) of 10,000 cells. Since the problem reduces to an ordinary differential equation, we prescribe the initial condition at $r = R_0$ (named the inlet condition U_{inlet}). Using the algorithms (39) or (40) whether u_θ is null or not, we obtain a numerical approximation on domain $[R_0, R_1]$ and we denote by U_{outlet} the solution at $r = R_1$.

To compute the non-stationary solution, we use a rectangular domain $\Omega = [0.1, 0.4] \times [0, 0.1]$ uniformly discretizated in quadrilaterals cut in two triangles (see Fig. 4). Table 1 gives the cell size for the meshes we have considered in the test.

We prescribe the reflection condition at the boundaries $z = 0$ and $z = 0.1$ and inlet and outlet conditions at the boundaries $r = R_0 = 0.1$ and $r = R_1 = 0.4$, respectively. We initialize the density in function of r with the expression (33) and we deduce the velocity and pressure approximations with relations (25) and (27) respectively. Two numerical experiments have been performed, the first one concerns the simple case where $u_\theta = 0$ and the second test deals with the general case which corresponds to the swirling flow.

5.2.1. Case $u_\theta = 0$

We use the numerical scheme (39) and impose the following inlet conditions at $r = R_0$. We compute all the variables of vector U at each point of the subdivision, in particular we obtain the outlet condition at $r = R_1$

$$C_{\text{inlet}} = \begin{pmatrix} \rho_{\text{inlet}} = 2 \\ u_{r,\text{inlet}} = 200 \\ u_{\theta,\text{inlet}} = 0 \\ u_{z,\text{inlet}} = 0 \\ P_{\text{inlet}} = 2 \times 10^5 \end{pmatrix}, \quad C_{\text{outlet}} = \begin{pmatrix} \rho_{\text{outlet}} = 2.283222 \\ u_{r,\text{outlet}} = 43.79776 \\ u_{\theta,\text{outlet}} = 0 \\ u_{z,\text{outlet}} = 0 \\ P_{\text{outlet}} = 2.407435 \times 10^5 \end{pmatrix}.$$

We now introduce the two boundary conditions in the non-stationary scheme and run until a stationary situation is achieved.

In order to measure the scheme accuracy and convergence to steady-state solution, we compute $\alpha_{1,i}$ and $\alpha_{3,i}$ given by relations (25) and (27) for each cell i and we define the L^2-norm error with

$$\alpha_{1,\text{error}} = \sqrt{\sum_i (\alpha_1 - \alpha_{1,i})^2 |C_i|_r}, \quad \alpha_{3,\text{error}} = \sqrt{\sum_i (\alpha_3 - \alpha_{3,i})^2 |C_i|_r},$$

while the L^∞-norm error is given by

Table 1
Mesh characteristics.

	Cell number/radial cell number	Mesh size h
Mesh 1	400/25	1.2×10^{-2}
Mesh 2	1600/50	6.0×10^{-3}
Mesh 3	6600/100	3.0×10^{-3}
Mesh 4	26,400/200	1.5×10^{-3}

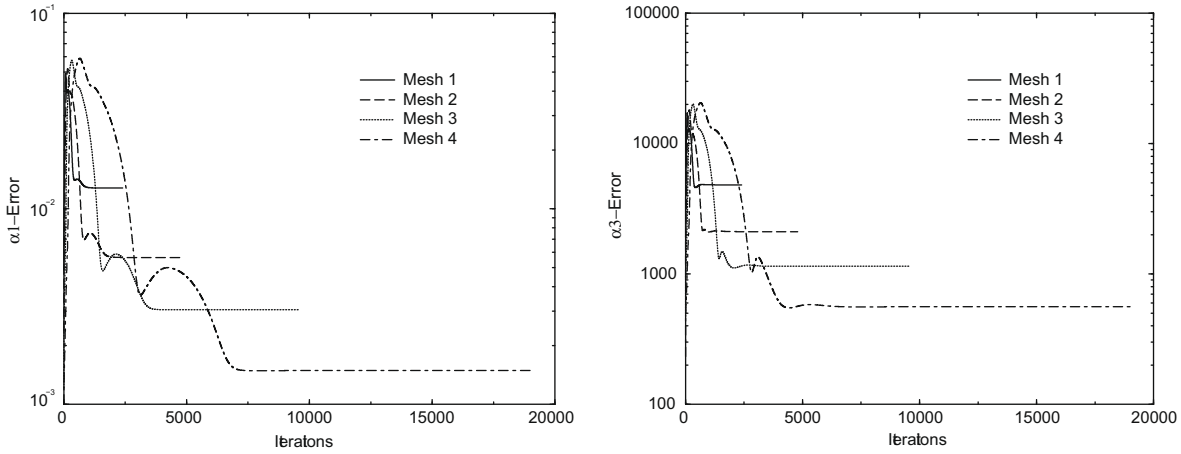

Fig. 5. History of error on α_1 (left) and α_3 (right) in L^2-norm with first-order HLLC scheme.

$$\alpha_{1,\text{error}} = \text{Max}(|\alpha_1 - \alpha_{1,i}|), \quad \alpha_{3,\text{error}} = \text{Max}(|\alpha_3 - \alpha_{3,i}|).$$

Note that $u_\theta = 0$ and relation (28) give $\alpha_2 = 0$. On the other hand, $\alpha_{1,\text{error}} = 0$ and $\alpha_{3,\text{error}} = 0$ imply that the steady-state solution is reached.

Figs. 5 and 6 present α_1 and $\alpha_3 L^2$-norm errors vs. the iteration number using the HLLC numerical flux with the first-order and the second-order schemes, respectively. We compare in Fig. 7 the density and the radial velocity distributions obtained by the first- and second-order HLLC scheme using mesh 3 with the exact solution. The two approximations of the steady-state solution are clearly close and the second-order scheme with the HLLC flux providing the best approximation.

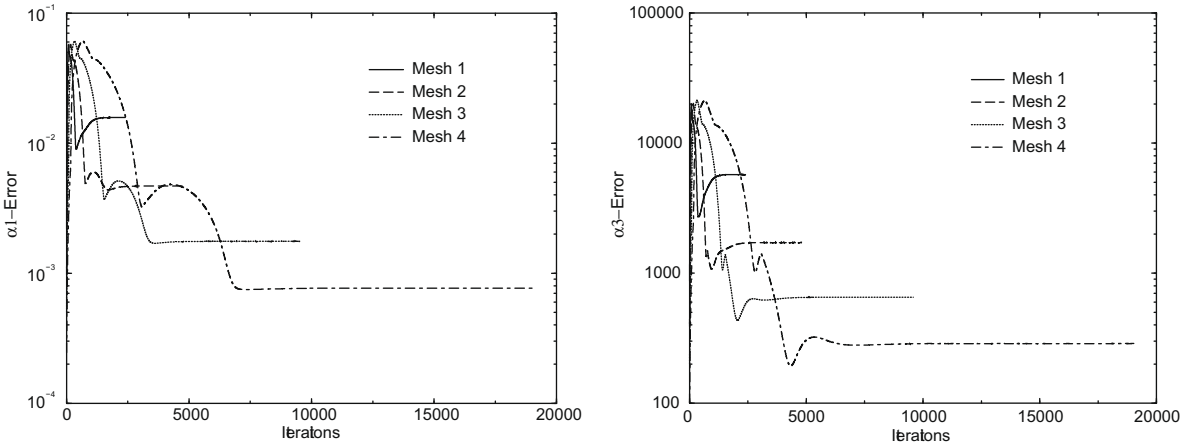

Fig. 6. History of error on α_1 (left) and α_3 (right) in L^2-norm obtained by second-order HLLC scheme.

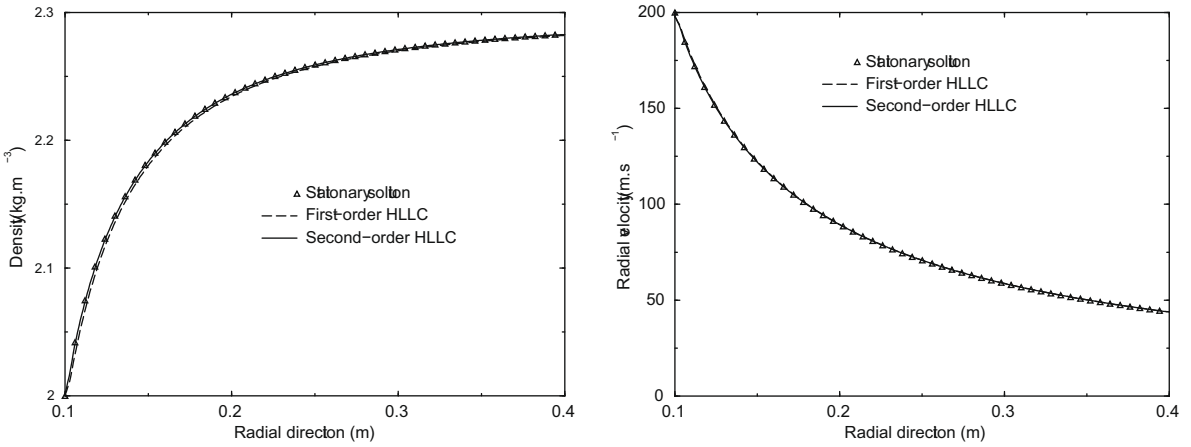

Fig. 7. Comparison of density and radial velocity distributions vs. radial direction at $z = 0.05$ between the stationary solution and numerical results for mesh 3.

Table 2
Convergence rate for α_1 in L^2-norm and L^∞-norm using first-order and second-order scheme (case $u_\theta = 0$).

h	1.2×10^{-2}	6.0×10^{-3}	3.0×10^{-3}	1.5×10^{-3}
First-order, L^2-norm	1.276e−02	5.632e−03	3.048e−03	1.489e−03
Order	–	1.27	0.92	1.02
Second-order, L^2-norm	1.573e−02	4.680e−03	1.756e−03	7.666e−04
Order	–	1.68	1.34	1.15
First-order, L^∞-norm	4.778e−01	2.503e−01	1.250e−01	6.208e−02
Order	–	0.95	1.00	1.00
Second-order, L^∞-norm	5.074e−01	1.978e−01	9.030e−02	4.464e−02
Order	–	1.28	1.09	1.01

Table 2 gives the convergence rate of α_1 in L^2-norm and L^∞-norm for the first-order and second-order methods using the HLLC numerical flux. We obtain an effective $O(h)$ for the first-order scheme but the second-order one does not achieve an effective $O(h^2)$. Nevertheless, the numerical approximations are really better when we use the second-order technique since the L^2-norm error is reduced by 50% with the finest mesh. Indeed, the ghost-cell technique we use to impose the boundary conditions deteriorates the second-order method in the vicinity of the boundary since the slope is cancelled for the sides sharing the boundary domain.

5.2.2. Case $u_\theta \neq q0$

We now deal with the swirling flow where we use the algorithm (40) and the new inlet and outlet conditions. With the two boundary conditions in hand, we compute the non-stationary solution until a stationary solution is obtained

$$C_{\text{inlet}} = \begin{pmatrix} \rho_{\text{inlet}} = 2 \\ u_{r,\text{inlet}} = 200 \\ u_{\theta,\text{inlet}} = 15 \\ u_{z,\text{inlet}} = 0 \\ P_{\text{inlet}} = 2 \times 10^5 \end{pmatrix}, \quad C_{\text{outlet}} = \begin{pmatrix} \rho_{\text{outlet}} = 2.284875 \\ u_{r,\text{outlet}} = 43.76607 \\ u_{\theta,\text{outlet}} = 3.75 \\ u_{z,\text{outlet}} = 0 \\ P_{\text{outlet}} = 2.409875 \times 10^5 \end{pmatrix}.$$

Figs. 8 and 9 give the history of the α_1, α_2 and α_3 errors using the L^2-norm for the four meshes. We print out in Fig. 10 the density and velocity components u_r and u_θ obtained with the third mesh using both first- and second-order scheme and the HLLC numerical flux. We observe a very good correspondence with the steady-state solution confirmed by the convergence orders given in Table 3. As in the previous case, we do not achieve an effective $O(h^2)$ when the reconstruction is employed but accuracy is higher and justify the use of the second-order method.

5.3. The Sod tubes

We divide the domain $\Omega = [0,1] \times [0,1]$ into two sub-domains $\Omega_L = [0,1] \times [0,\frac{1}{2}]$ and $\Omega_R = [0,1] \times [\frac{1}{2},1]$ parted with the line $D = \{(r,\frac{1}{2});\ r \in [0,1]\}$. We then consider the shock tube problem prescribing the initial condition $U(t=0) = U_L$ in Ω_L and $U(t=0) = U_R$ in Ω_R where we impose the reflection condition at the boundary $r = 1$ of Ω and the Dirichlet condition

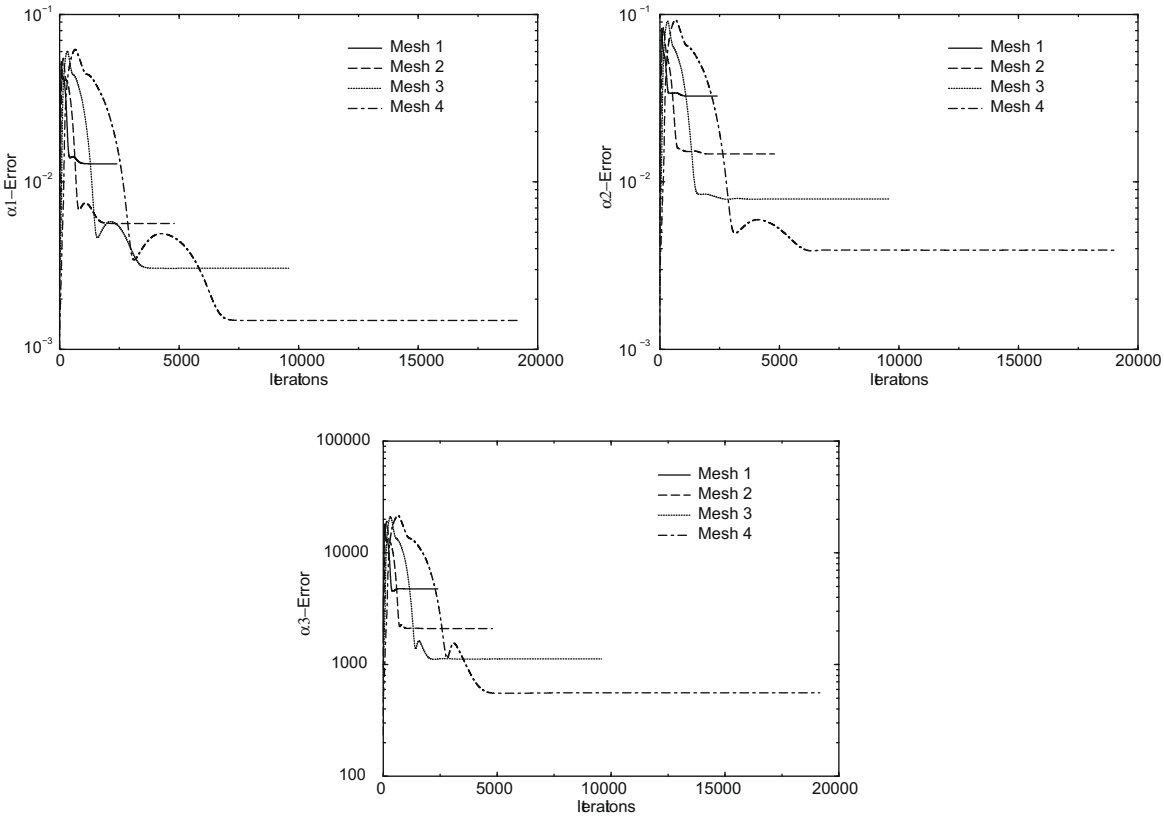

Fig. 8. History of error on α_1, α_2 and α_3 using first-order scheme with HLLC numerical flux.

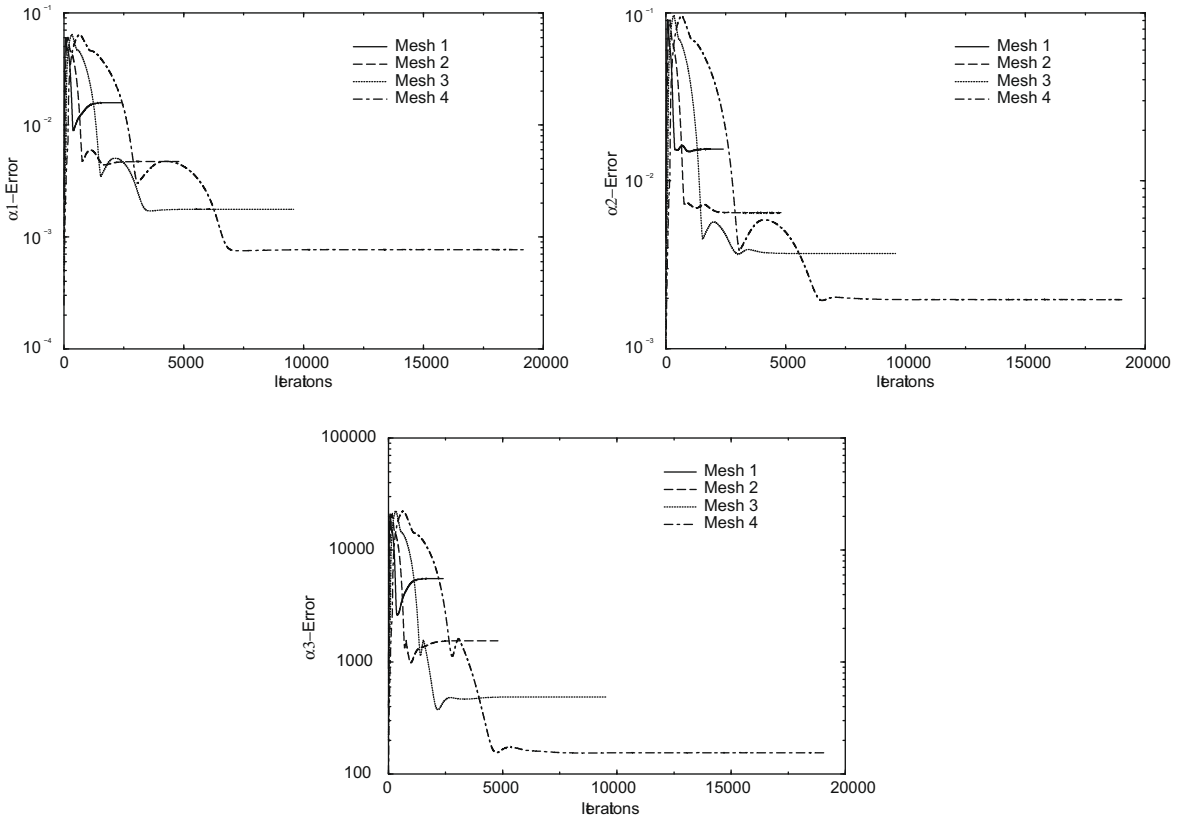

Fig. 9. History of error on α_1, α_2 and α_3 using second-order scheme and HLLC numerical flux.

$U(t, r, z = 0) = U_L, U(t, r, z = 1) = U_R$. Such a geometry and initial conditions lead to a solution invariant with respect to r and we obtain a classical one-dimensional shock tube problem in the Oz direction with an initial discontinuity at $z = 1/2$. All the computations have been performed with triangulation meshes similar to Fig. 4 composed of 100 (coarse mesh) or 200 (fine mesh) subdivisions on the axial direction divided in two triangles, the initial discontinuity line D fitting the discretizations.

We have tested three classical Riemann problems given in ([18, p. 129]): Test 1 is the so-called Sod test problem where the solution consists of a left rarefaction, a contact discontinuity and a right shock. Test 2 represents a left and a right shock with a contact discontinuity moving to the right. Test 3 consists of two symmetric strong rarefactions and a stationary contact discontinuity where the solution involves a state close to the vacuum. We summarize in Table 4 the left and right initial states for each problem and Table 5 gives the exact intermediate states.

We present in Fig. 11 a comparison of the density and internal energy between the exact solution and the approximations using the Rusanov and HLLC flux with the first-order scheme for Test 1 while Fig. 12 shows a similar comparison using the second-order MUSCL technique. The solutions are in good agreement with the exact solution and the second-order scheme provides the better approximations by reducing the diffusion effect close to the discontinuities. We also remark that the Rusanov and HLLC schemes provide the same approximation quality in the second-order context whereas the HLLC flux is less diffusive with the first-order scheme.

For Tests 2 and 3, we compute the solution approximations with the algorithm dedicated to axisymmetric geometries using the second-order HLLC scheme where we use three limiters (minmod, van Albada and van Leer). The density and the internal energy curves are presented in Figs. 13 and 14. The numerical results are similar for the density but important differences of accuracy are noticeable for the internal energy close to the vacuum where the van Albada and van Leer limiters give the best approximations.

5.4. Converging spherical shock test

In $\mathbb{R}^3$, a spherical bubble of gas, with radius R, centered at the origin is compressed by an over-pressured exterior gas of same nature. The solution involves the three classical waves and depends only on the spherical radius R, i.e. $U(r, z) = U(R, 0) = U(0, R)$ for any point (r, z) such that $R^2 = r^2 + z^2$. To treat the spherical bubble problem with the axisymmetric model, we can choose arbitrarily the Or and Oz axes, the main difficulty being that the variables r and z do not play the

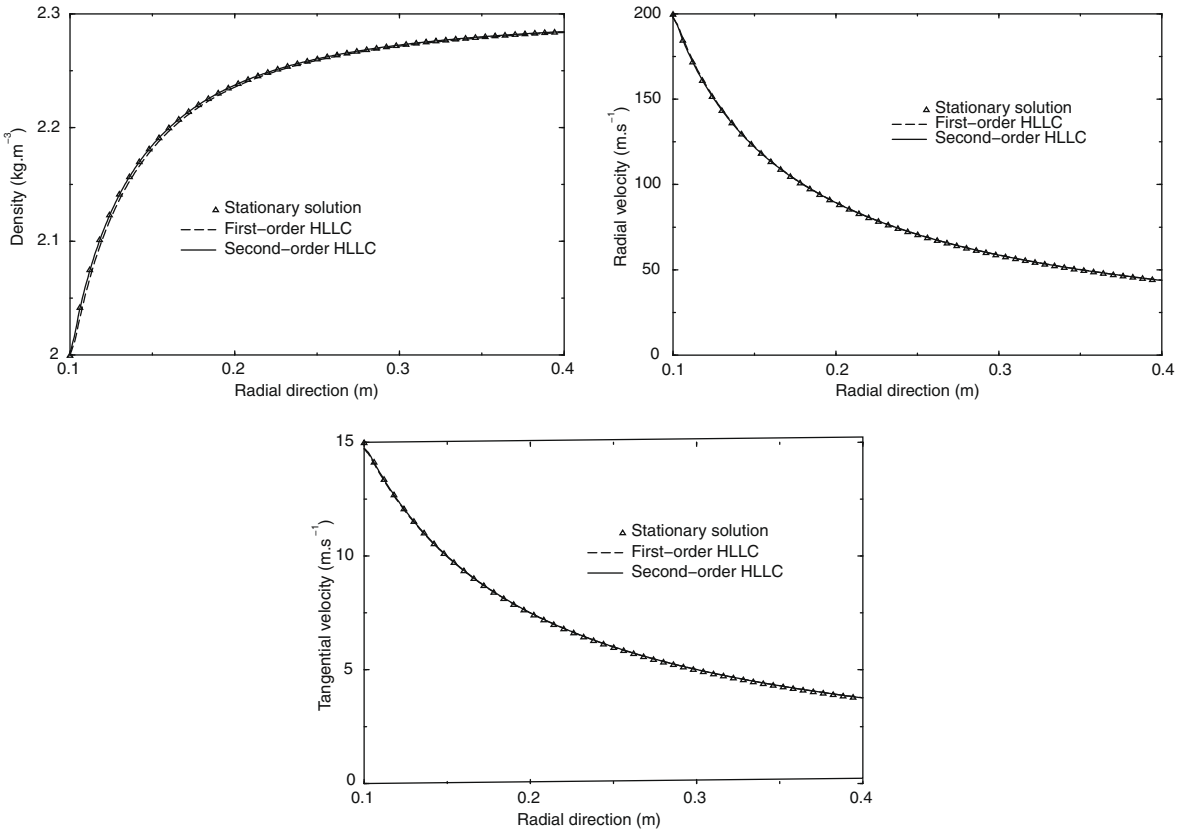

Fig. 10. Comparison of density, radial and tangential velocity distributions vs. radial direction between the stationary solution and numerical results using mesh 3.

Table 3
Convergence rate for α_1 in L^2-norm and L^∞-norm using first-order and second-order scheme (case $u_\theta \neq 0$).

h	1.2×10^{-2}	6.0×10^{-3}	3.0×10^{-3}	1.5×10^{-3}
First-order, L^2-norm	1.280e−02	5.640e−03	3.053e−03	1.491e−03
Order	–	1.13	0.92	1.02
Second-order, L^2-norm	1.577e−02	4.694e−03	1.762e−03	7.681e−04
Order	–	1.68	1.33	1.15
First-order, L^∞-norm	4.784e−01	2.508e−01	1.252e−01	6.223e−02
Order	–	0.95	1.00	1.00
Second-order, L^∞-norm	5.104e−01	1.961e−01	9.049e−02	4.477e−02
Order	–	1.30	1.08	1.01

Table 4
Data for three Riemann problem tests.

Test	ρ_L	u_L	P_L	ρ_R	u_R	P_R
1	1.0	0.0	1.0	0.125	0.0	0.1
2	5.99924	19.5975	460.894	5.99242	−6.19633	46.0950
3	1.0	−2.0	0.4	1.0	2.0	0.4

same role in the axisymmetric formulation. The goal of this test is to study the asymmetry of the solution following the *Or* and *Oz* axes.

To simulate the spherical bubble compression using the axisymmetric model, we consider a quarter of disk

$$D = \left\{ (r,z);\ \sqrt{r^2+z^2} \leqslant \frac{1}{2} \right\}$$

Table 5
Exact solution for pressure, velocity and densities for Tests 1, 2 and 3.

Test	P^*	u^*	ρ_{*L}	ρ_{*R}
1	0.30313	0.92745	0.42632	0.26557
2	1691.64	8.68975	14.2823	31.0426
3	0.00189	0.0	0.02185	0.02185

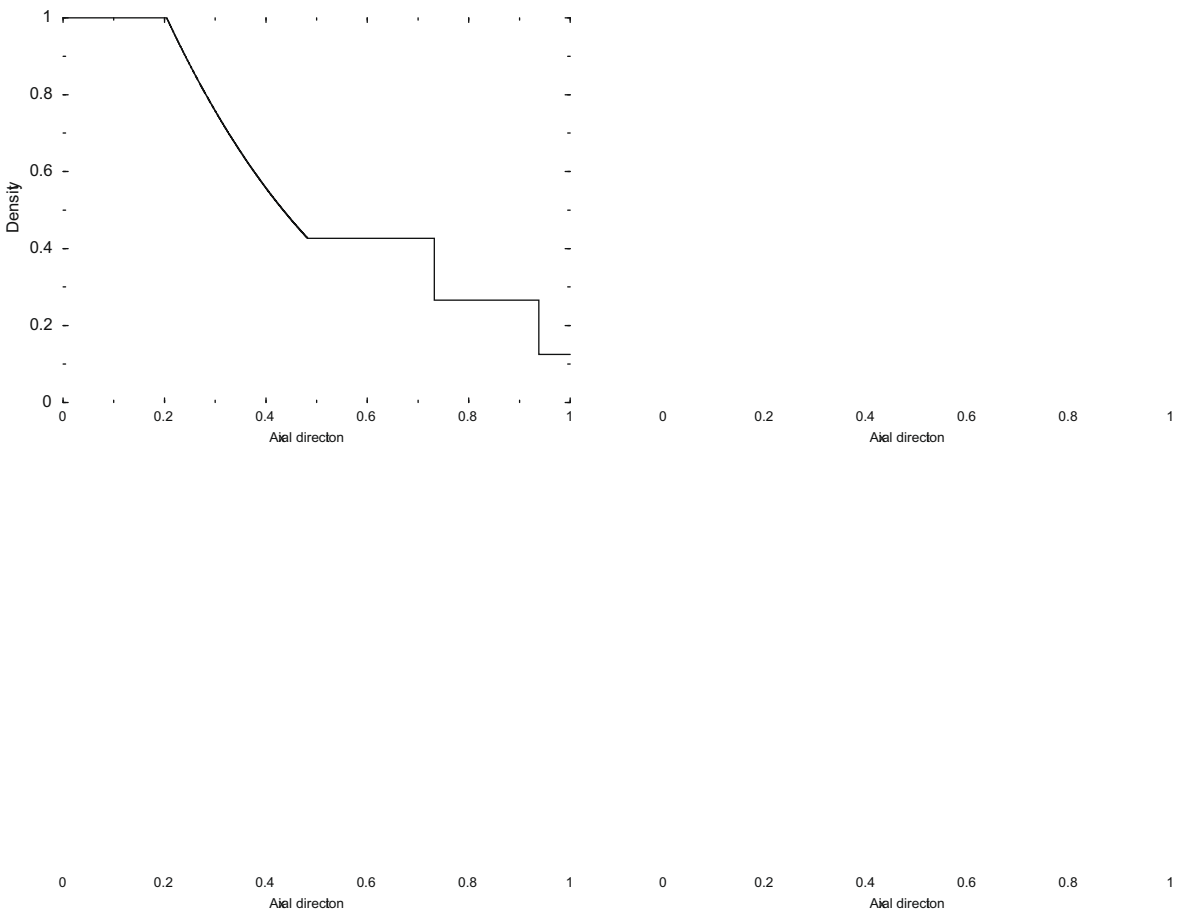

in the unit square $\Omega = [0,1] \times [0,1]$ and we enforce the following initial conditions:

$$(\rho, u_r, u_z, u_\theta, P) = \begin{cases} (1,0,0,0,1) & \text{in } D, \\ (4,0,0,0,4) & \text{in } \Omega \setminus D. \end{cases}$$

We also prescribe reflecting boundary conditions on the whole boundary. We have performed numerical tests with a discretization of the domain into 20000 finite volume cells where we use a 100×100 uniform quadrilateral mesh cut into triangles as in Fig. 4.

In Fig. 15 we present the density distribution at time $t = 0.2$ using second-order Rusanov and HLLC fluxes. Both choices provide very similar numerical solutions and we observe a small asymmetry confirmed by the visualization of the density value along the Or and Oz axis in Fig. 16.

In addition, we plot in Fig. 17 the density along $r = z$ using second-order HLLC scheme with three limiters and we observe very few differences between the three limiters for this particular test.

5.5. Supersonic channel flow

We present a comparison of the axisymmetric/two-dimensional Euler equations using second-order Rusanov and HLLC schemes. For the two-dimensional situation, the geometry corresponds to a channel with a 10-degree oblique step while

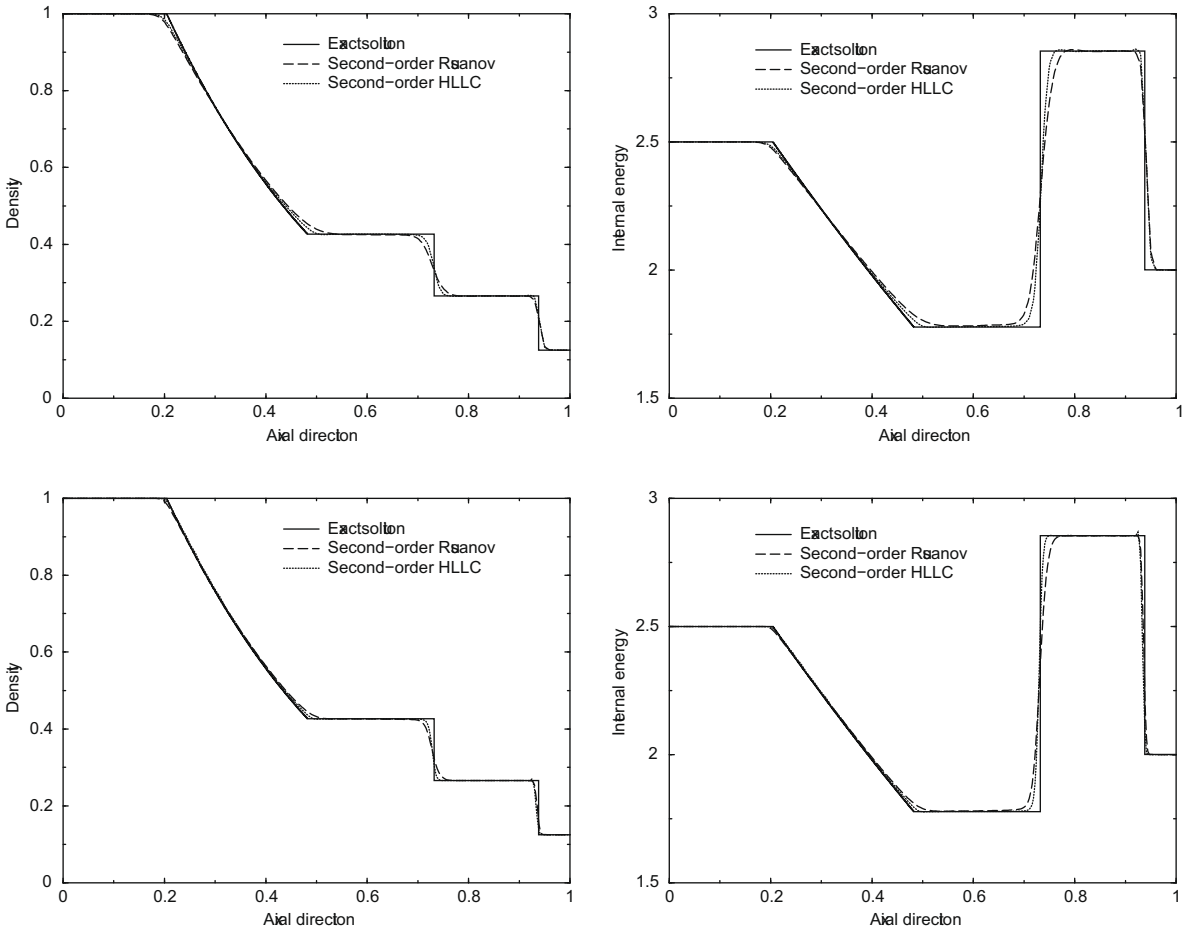

Fig. 12. Density and internal energy obtained by second-order Rusanov and HLLC schemes and exact solution at $t = 0.25$ units for Test 1 using a mesh of 100 cells (top) and 200 cells (bottom) following the z-direction.

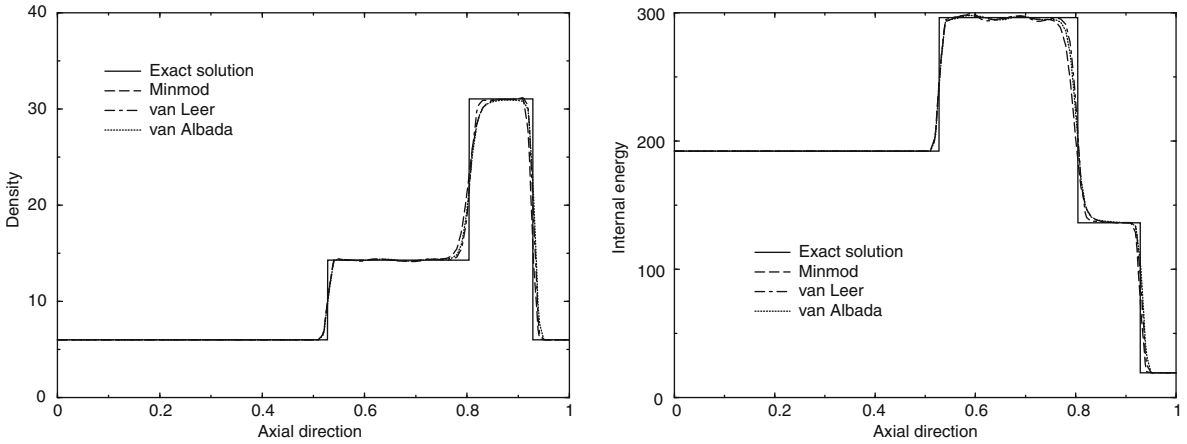

Fig. 13. Density and internal energy for second-order HLLC scheme testing three limiters and exact solution at time $t = 0.035$ units for Test 2.

the geometry corresponds to a cone located inside a tube in the axisymmetric situation (see [12, p. 201] for geometry details). Both compression and expansion appear at the corners illustrating the formation of oblique shock and expansion waves and their reflection and interaction. To perform the simulations, we use an unstructured coarse Delaunay mesh of 5176 elements and a finer mesh of 20,785 elements. A supersonic flow is applied at the entry (left) of the channel and

the free stream pressure and density are 10^5 Pa and 1.16 kg m^{-3}, respectively. Solution is calculated for a free stream Mach number of $M_\infty = 2.0$. In addition we have realized the same test using a tangential velocity $u_\theta = 200r$ to produce a swirling flow.

In order to measure convergence to the steady state solution, we compute the L^2–norm of the pressure residual:

$$\text{CONV} = \sqrt{\sum_i (P_i^{n+1} - P_i^n)^2 |C_i|_r}.$$

History curves of the pressure residual are given in Fig. 18. We note a good convergence behavior of the numerical scheme when the Rusanov flux is employed for both two-dimensional and axisymmetric codes. In contrast, convergence has poor behavior with HLLC flux in the axisymmetric situation.

For the two-dimensional geometry, density contours show the formation of an oblique shock, an expansion wave and their reflection and interaction (see [12, p. 207]). We have similar wave development but the oblique shock is smoothed as in Désidéri and Goudjo [6] in the axisymmetric configuration (see Fig. 19 (middle)). We perform the same numerical simulation with the finest mesh (see Fig. 19 (bottom)) and we obtain a flow structure very similar to the one using the coarse mesh.

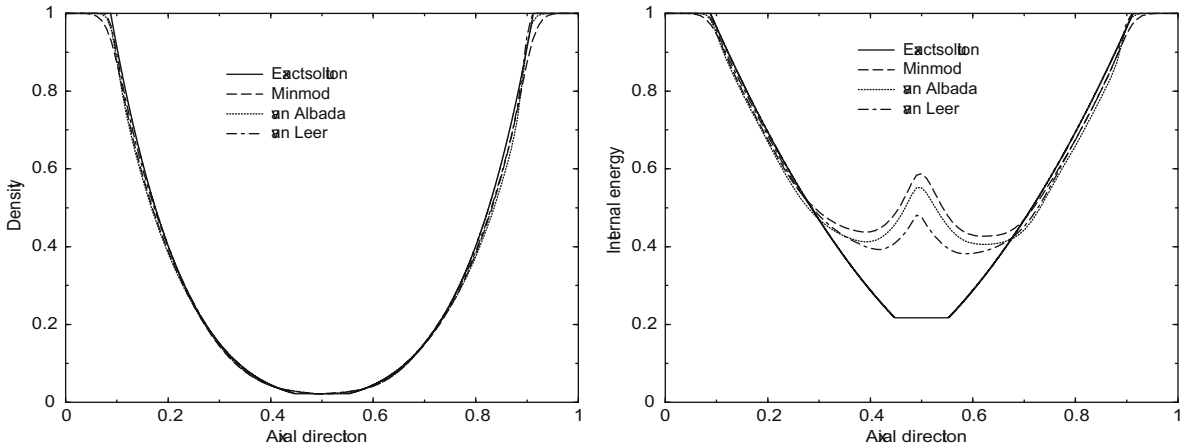

Fig. 14. Density and internal energy for second-order HLLC scheme testing three limiters and exact solution at time $t = 0.15$ units for Test 3.

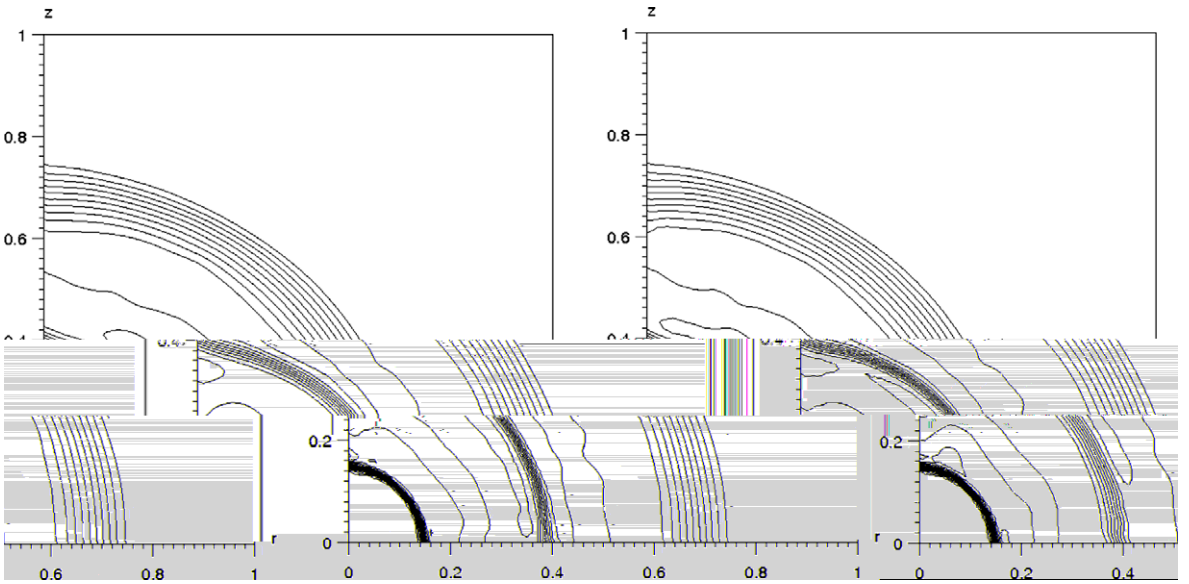

Fig. 15. Density at $t = 0.2$, 31 contours from 1 to 4 for second-order Rusanov (left) and HLLC scheme (right).

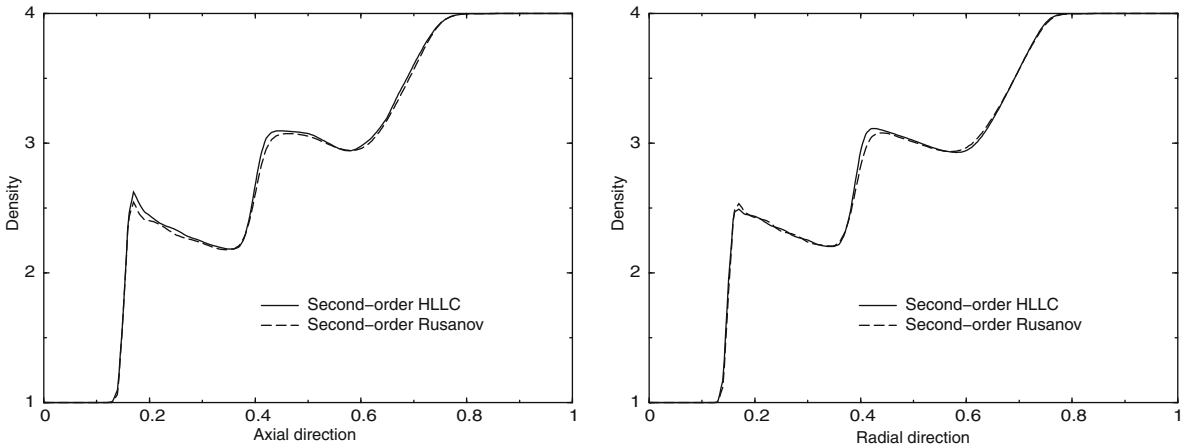

Fig. 16. Comparison of density at $t = 0.2$ for $r = 0$ (left) and $z = 0$ (right).

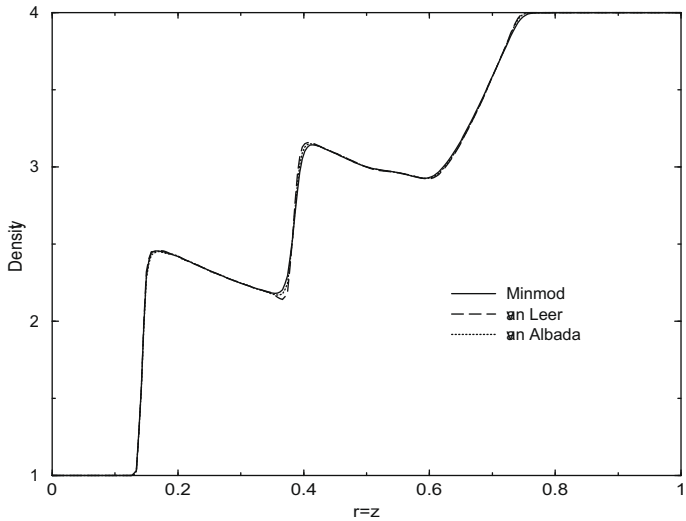

Fig. 17. Density along the line $r = z$ with second-order HLLC scheme and three limiters.

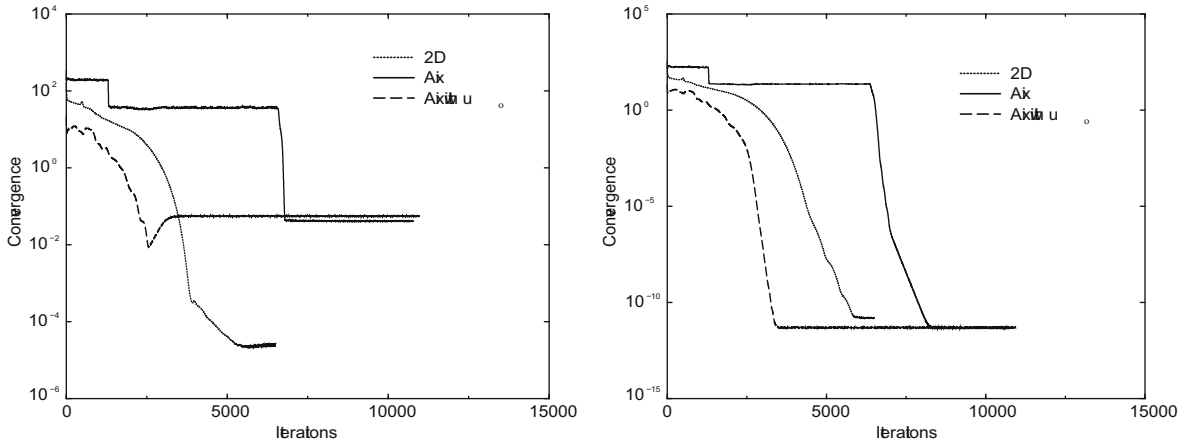

Fig. 18. The supersonic channel flow: convergence criterion with HLLC flux (left) and Rusanov flux (right) vs. iterations (second-order scheme with coarse mesh).

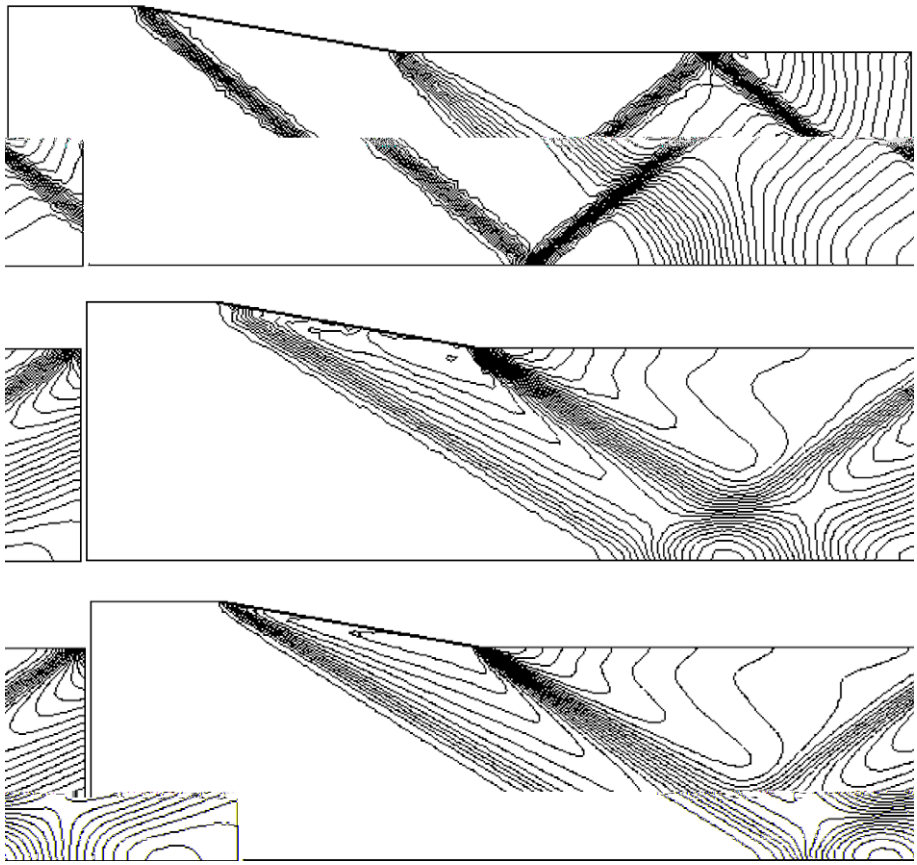

Fig. 19. Density contours for $M_\infty = 2$ using 2D geometry (top), max: 2.41, min: 1.15 and axisymmetric geometry with $u_\theta = 0$ with 5176 elements (middle), max: 1.48, min: 0.98 and 20,785 elements (bottom) max: 1.5, min: 0.97.

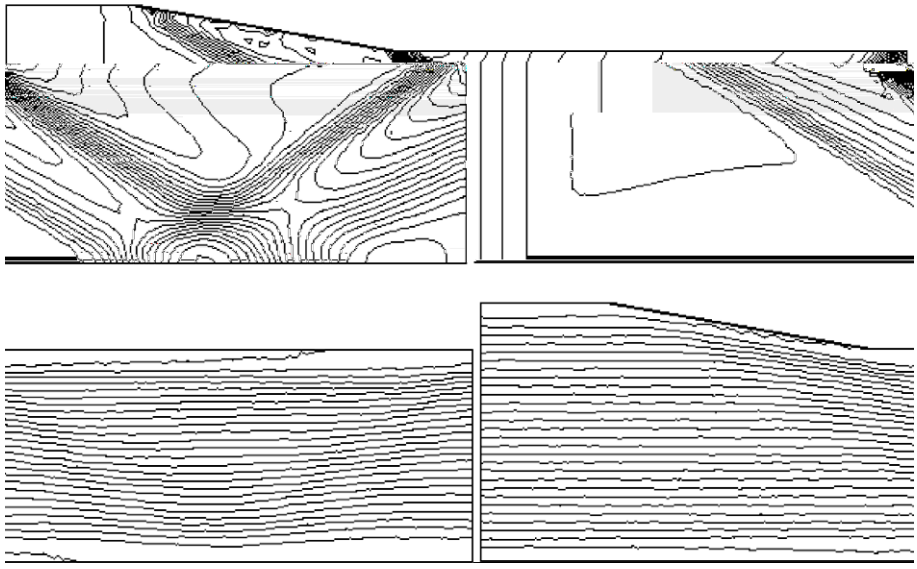

Fig. 20. Density contours (top) max: 1.47, min: 0.98 and tangential velocity contours (bottom), max: 40, min: 0 for $M_\infty = 2$ using axisymmetric geometry, 5176 elements with $u_\theta = 200r$.

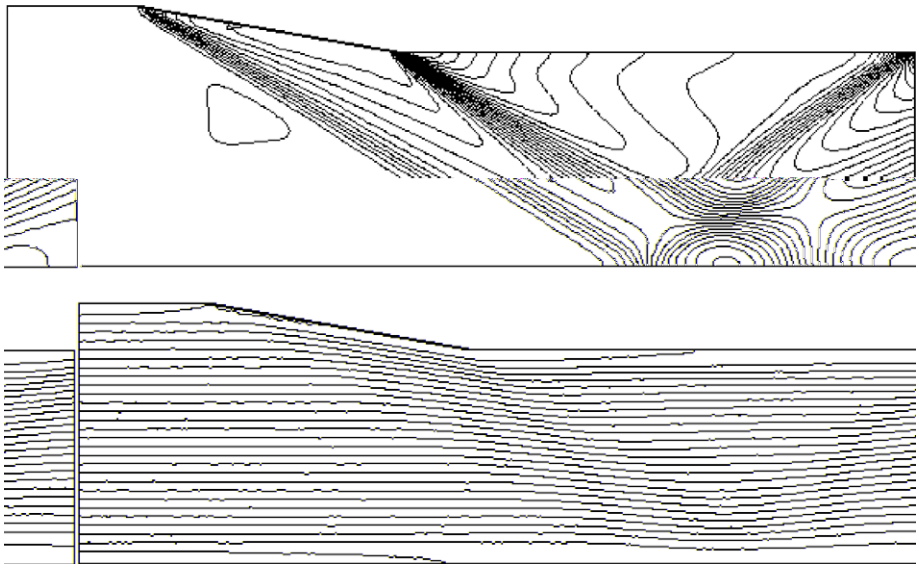

Fig. 21. Density contours (top) max: 1.48, min: 0.96 and tangential velocity contours (bottom), max: 39.6, min: 0.37 for $M_\infty = 2$ using axisymmetric geometry with 20,785 elements with $u_\theta = 200r$.

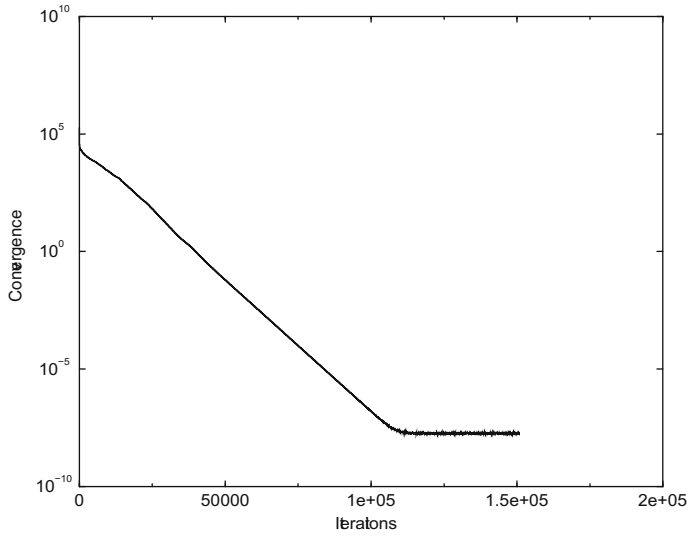

Fig. 22. Pressure residual error for the axisymmetric blunt body with a free stream Mach number $M_\infty = 18$, using Rusanov flux and second-order scheme.

We consider the same flow but with an additional swirl velocity given by $u_\theta = 200r$. We note a small perturbation for the density and the swirl velocity contours in Figs. 20 and 21 has roughly a linear behavior in r. We also perform the simulation using the finest mesh to check the convergence. In the present configuration, the swirl velocity does not deeply change the flow structure. Indeed, Eq. (13) shows that the u_θ component is convected by the velocity (u_r, u_z) where the axial velocity u_z does not depend on u_θ and only the radial velocity would be affected by the centrifugal force and change the flux structure. We use the same dimension as in Hoffmann and Chiang [12, p. 205] where the greater radius is 0.2. We deduce that the centrifugal force f_{cen} is at most

$$f_{cen} = \rho u_\theta^2 \approx 1.16 \times (0.2 \times 200)^2 \leqslant 2000.$$

In Eq. (11), the centrifugal force is added to the pressure but $P \gg f_{cen}$ hence the centrifugal force impact is negligible. It results that, in the present application, the velocity field (u_r, u_z) is not perturbed by the swirl flow.

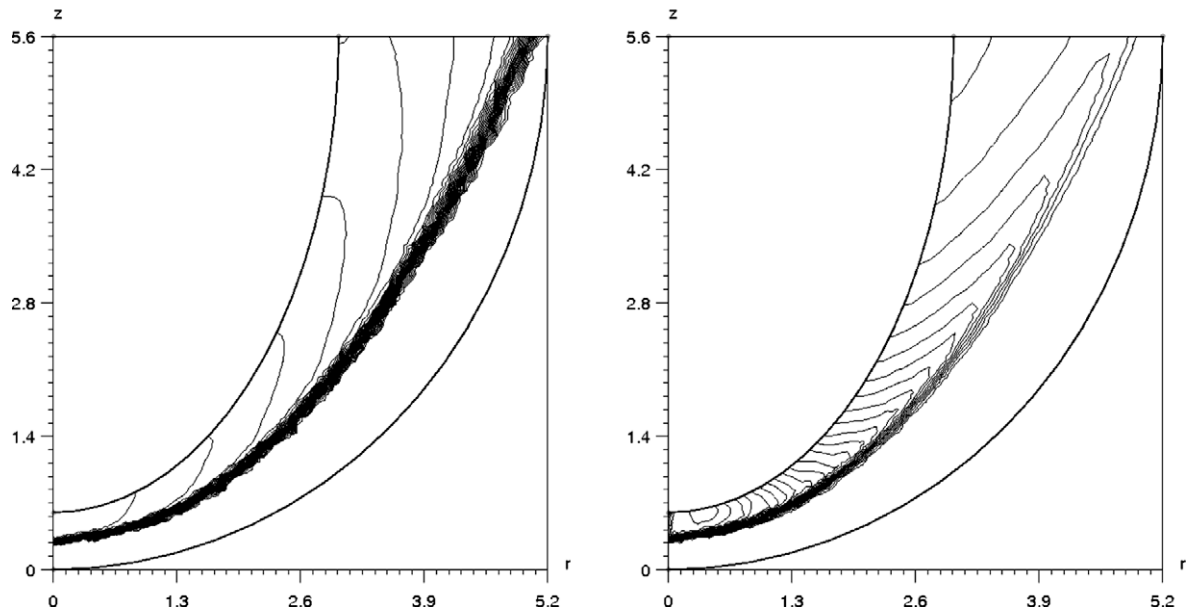

Fig. 23. Mach contours (left) with 30 Mach isolines: max: 18, min: 0.05 and 30 pressure isolines: max: 4.1×10^7, min: 1.0×10^5 for the axisymmetric blunt body with a free stream Mach number $M_\infty = 18$.

5.6. Axisymmetric blunt body

We consider an axisymmetric blunt body defined geometrically by an ellipse (see [12, p. 210] for the geometry details). We assume a hypersonic flow field where the free stream Mach number is 18. We compute the steady-state inviscid flow using the second-order Rusanov scheme on a coarse Delaunay mesh of 5289 elements. Fig. 22 shows that a convergent solution is obtained after 10^5 iterations and we print out in Fig. 23 the Mach and pressure isolines. We obtain a very similar structure flow in comparison to the one given in Hoffmann and Chiang [12, p. 213] and the simulation demonstrates the applicability of the scheme to handle high-Mach flow. The detached bow shock near the $r = 0$ axis is smoothed in a small layer of two cells length and the shock position corresponds to the one proposed in Hoffmann and Chiang [12]. The carbuncle phenomenon (a spurious bump on the bow shock in front of the body see [17] or [16]) does not appear since the Rusanov flux do not preserve the contact discontinuities [7].

6. Conclusion

We have proposed a new second order cell-centered finite volume formulation for compressible Euler equations using cylindrical coordinates to compute axisymmetric solutions. The finite volume scheme is based on a mean value approximation using the $rdrdz$ metric instead of the traditional $drdz$ metric to simplify the boundary condition on the Or axis. An original MUSCL method (multislope MUSCL method) is introduced where an estimate of the directional derivatives is performed to construct more accurate approximations of the solution on both sides of edges. New numerical tests based on the steady-state situation has been proposed to validate the numerical scheme and to compare different scheme performances.

References

[1] P. Batten, N. Clarke, C. Lambert, D.M. Causon, On the choice of wavespeeds for the HLLC Riemann solver, SIAM J. Sci. Comput. 18 (6) (1997) 1553–1570.
[2] T. Buffard, S. Clain, Monoslope and multislope MUSCL methods for unstructured meshes, J. Comput. Phys. 229 (2010) 3745–3776.
[3] S. Clain, V. Clauzon, The multislope MUSCL method, in: Proceeding in the Finite Volumes for Complex Application, vol. 5, Wiley, 2008, pp. 297–304.
[4] V. Clauzon, Analyse de Schémas d'ordre élevé pour les écoulements compressibles.t Application à la simulation numérique d'une torche à plasma, Ph.D. Thesis, Blaise Pascal University, Clermont Ferrand, 2008. <http://tel.archives-ouvertes.fr/tel-00235951/fr>.
[5] R. Cumming, H. Yang, Y. Oh, Supersonic, turbulent flow computation and drag optimization for axisymmetric afterbodies, Comput. Fluids 24 (1995) 487–507.
[6] J.A. Désidéri, A. Goudjo, Un schéma de volumes-finis décentré pour la résolution des équations d'Euler en axisymétrique, INRIA Report No. 1005, 1989.
[7] M. Dumbser, J. M Moschetta, J. Gressier, A matrix stability analysis of the carbuncle phenomenon, J. Comput. Phys. 197 (2004) 647–670.
[8] P. Glaister, Flux difference splitting for the Euler equations with axial symmetry, J. Eng. Math. 22 (1988) 107–121.
[9] E. Godlewski, P.-A. Raviart, Hyperbolic Systems of Conservations Laws, Applied Mathematical Sciences, Springer, Berlin, 1995.
[10] A. Guardone, L. Vigevano, Finite element/volume solution to axisymmetric conservation laws, J. Comput. Phys. 224 (2) (2007) 489–518.
[11] Ch. Hirsch, G. Warzee, A finite element method for the axisymmetric flow computation in a turbomachine, Int. J. Numer. Meth. Eng. 10 (1) (1976) 93–113.

[12] K.A. Hoffmann, S.T. Chiang, Computational Fluid Dynamics, fourth ed., vol. II, Engineering Education System, Wichita, 2004.
[13] M.E. Hubbard, Multidimensional slope limiters for MUSCL-type finite volume schemes on unstructured grids, J. Comput. Phys. 155 (1999) 54–74.
[14] P.A. Jacob, Transient, Hypervelocity Flow in an Aaxisymmetric Nozzle, ICASE Report No 91-1, NASA Research Center, 1991.
[15] M.A. Leschziner, W. Rodi, Computation of strongly swirling axisymmetric free jets, AIAA J. 22 (1984) 1742–1747.
[16] M. Pandolfi, D. D'Ambrosio, Numerical instabilities in upwind methods: analysis and cures for the carbuncle phenomenon, J. Comput. Phys. 166 (2) (2001) 271–301.
[17] S. Phongthanapanich, P. Dechaumphai, Flux-difference splitting scheme with modified multidimensional dissipation on unstructured meshes, J. Chin. Inst. Eng. 27 (1) (2004) 981–992.
[18] E.F. Toro, Riemann Solvers and Numerical Methods for Fluid Dynamics, second ed., A Practical Introduction, Springer-Verlag, Berlin, 1999.
[19] R. Touzani, OFELI, An Object Finite Element Library, Rachid Touzani, Copyright ©1998–2009. <http://www.ofeli.net>.
[20] D.V. Vanden Abeele, G. Degrez, Efficient computational model for inductive plasma flows, AIAA J. 38 (2) (2000) 234–242.
[21] B. Van Leer, Towards the ultimate conservative difference scheme. V. A second-order scheme to Godunov's method, J. Comput. Phys. 32 (1) (1979) 101–136.
[22] S.A. Vasil'evskii, A.F. Kolesnikov, Numerical simulation of equilibrium induction plasma flows in a cylindrical plasmatron channel, Fluid Dyn. 35 (2000) 769–777.
[23] C.H. Wu, A General Theory of Three-dimensional Flow in Subsonic and Supersonic Turbomachine in Radial, Axial and Mixed Flow Types, NACA TN 2604, 1952.
[24] S. Xue, P. Proulx, M.I. Boulos, Extended-field electromagnetic model for the inductively coupled plasma, J. Phys. D: Appl. Phys. 34 (2001) 1897–1906.